A review of 'synoptic to intraseasonal' tropical waves with relevance to forecasting

Matthew C. Wheeler

Climate Forecasting Group, Bureau of Meteorology Research Centre

P.O. Box 1289K, Melbourne, VIC, 3001, Australia

M.Wheeler@bom.gov.au

1. Introduction

It has long been known that an important part of the synoptic and larger-scale variability in the Tropics is due to propagating disturbances moving in the zonal direction. Such disturbances organize individual convective elements on a spatial scale that is larger than the size of the elements themselves. A well-known example are the westward moving synoptic-scale disturbances within the intertropical convergence zones that were visible in time-longitude plots of cloudiness viewed from early satellites (e.g., Fig. 1, as taken from Chang 1970). Another well known example, but on an even larger scale, is the Madden-Julian oscillation, that is often observed as a continental-scale organization of convection moving slowly to the east across the Indian and western Pacific ocean regions. Collectively, all such propagating disturbances are commonly known as 'tropical waves', and this paper reviews some of the characteristics of the larger-scale tropical waves known from observations, as well as presenting a technique for diagnosing and forecasting them in real time.

For this purpose, I rely heavily on the data analysis techniques of spectral analysis and filtering. The paper is not intended as a complete review of the scientific literature, but instead draws mostly upon my own research and perspective of the current state of knowledge. References to theory will mostly be made to the standard text books on atmospheric dynamics only, for example, Gill (1982) and Holton (1992).

2. Spectral analysis

Spectral analysis is used commonly in the study of weather and climate data for identifying any oscillations or dominant scales of variability that may exist. When spectral analysis is performed on a data series it essentially transforms the series into a set of new quantities that describe the amplitude of each of the harmonics of the series, that is, it looks at the contributions made at different scales. For example, a long time series of hourly temperature data will usually exhibit strong variations both at the daily time scale (corresponding to the diurnal cycle of solar heating) and at the annual time scale (reflecting the annual solar cycle). In this paper we are interested in time scales between these extremes, that is, the synoptic to intraseasonal.

a. Frequency spectrum for the Madden-Julian oscillation

An example of a spectrum of a meteorological quantity in the tropics is presented in Fig. 2. Shown is the spectral power for pressures recorded at Nauru Island in the late 1800s. Only the power for frequencies corresponding to a period of 14 days up to a period of 360 days is shown. In general, the power spectrum is quite 'red' in character, with the most power (per unit bandwidth) occurring for the lowest frequencies. This is a common characteristic of most geophysical time series, and is especially the case in this time series when one notes that the power is plotted on a logarithmic scale. Besides this 'redness', the spectrum also shows a prominent and wide local maximum in the period range of about 30 to 60 days (with an absolute peak at around 40–50 days). This spectral maximum, or 'peak', indicates that there is an inclination (at least during 1894–1898) for the pressure at Nauru to oscillate with periods somewhere between 30 and 60 days, and this inclination occurs more often, or with greater amplitude, than for oscillations with periods outside this range (e.g. at periods of 100 days or 14 days).

Tests of statistical significance may be applied to power spectra to determine whether a spectral peak is significantly different from that which could be produced by noise. In the case of the power spectrum at Nauru (Fig. 2), a comparison to a red noise background spectrum, that is, one that is continuously increasing
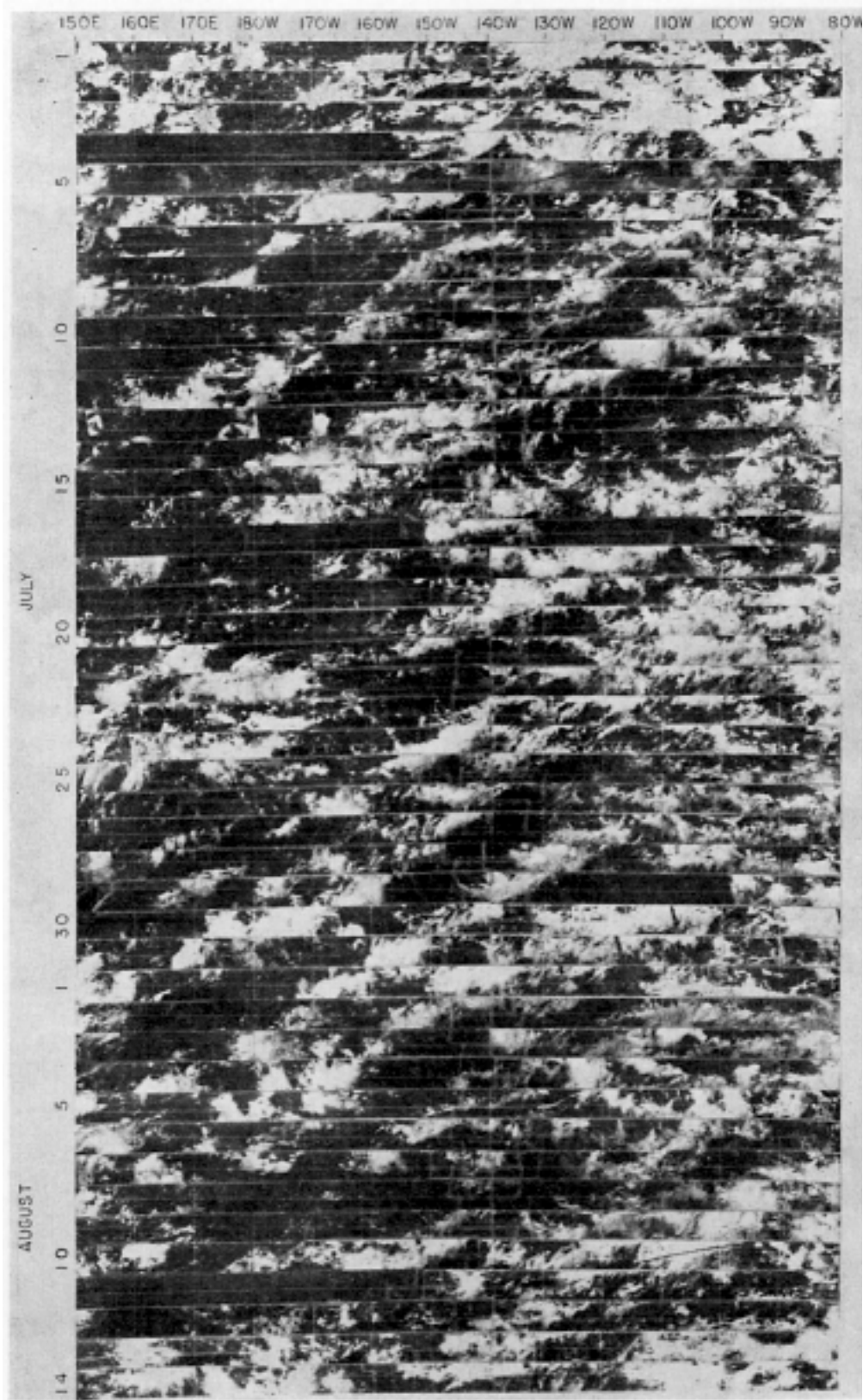
FIG. 1: Time-longitude section of satellite photographs of the period 1 July–14 August 1967 for the 5–10°N latitude band in the Pacific. The westward progression of the cloud clusters is indicated by the bands of cloudiness sloping down the page from right to left (taken from Chang 1970).
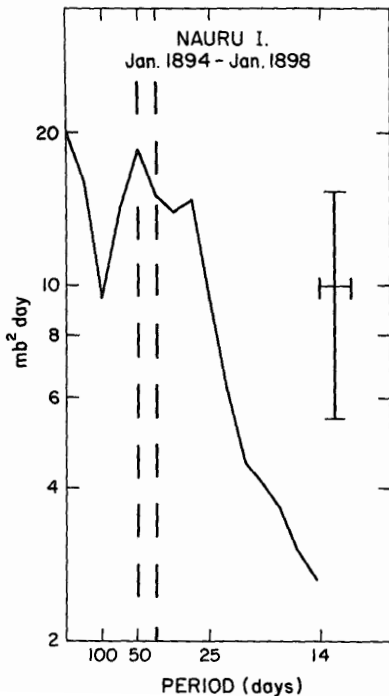
FIG. 2: Power spectrum for station pressures at Nauru Island, 0.4°S, 161.0°E. Ordinate (variance per interval of frequency) is logarithmic and abscissa (frequency) is linear. The 40–50-day period range is indicated by the dashed vertical lines. Prior 95% confidence limits and the bandwidth of the analysis (0.008 day^{-1}) are indicated by the cross (taken from Madden and Julian 1972).

with decreasing frequency (i.e., sloping up to the left), makes the most sense. What actually constitutes the background power spectrum can only be estimated, and in the case of Fig. 2, it would be reasonable to estimate it as a straight line sloping down to the right, passing near the local minimum in the spectrum at a period of 100 days, and along the part of the spectrum near a period of around 20 days. The spectral peak between 30 and 60 days would evidently be much above such a background spectrum, and as has been shown by many researchers (the first being Madden and Julian, 1971 and 1972), such a spectral peak in the data is both statistically significant (i.e., to a high degree of confidence it could not have occurred by chance) and robust (i.e., it appears in the analysis of a number of different meteorological variables, for stations throughout the tropical Indian Ocean to western Pacific regions, and for any period spanning at least a few years). The phenomenon contributing to this spectral peak is called the Madden-Julian oscillation or MJO. We now know it to be a very important mode of intraseasonal variability in the tropics. It is also known to be a propagating disturbance to the east, thus it can be called a tropical wave.

b. *Wavenumber-frequency spectra of clouds*

Spectral analysis can also be performed in two dimensions. If the input dimensions are longitude and time (e.g., as in Fig. 1), the output spectrum is a function of both zonal wavenumber and frequency. Such an analysis is quite useful for the study of zonally-propagating waves because it decomposes the longitude-time field into spectral components separately for eastward and westward propagating waves.

Fig. 3 shows a wavenumber-frequency spectral analysis of a long time-series of tropical outgoing long-wave radiation (OLR) data, a good indicator of cloudiness and moist convection in the tropics. As I will discuss, these figures form a good summary of the different time and space scales of variability acting in the tropics. Prior to calculating the spectra, the data were separated into antisymmetric and symmetric components about the equator. They are defined as $OLRA(\phi) = [OLR(\phi) - OLR(-\phi)]/2$ and $OLRS(\phi) = [OLR(\phi) + OLR(-\phi)]/2$, respectively, where ϕ is the latitude and $-\phi$ is the latitude on the opposite side of the equator. The original total field can be reconstructed as $OLR(\phi) = OLRA(\phi) + OLRS(\phi)$. This separation has been done because, as it turns out, many of the tropical waves that can be discerned in the data can be related to the theoretical equatorial waves, and these are either symmetric or antisymmetric about the equator. The power is thus displayed separately for each of these components, summed over the latitudes of 15°S to 15°N. The display in Fig. 3 is also such that eastward propagating components are defined to have positive wavenumber (i.e., on the right of each panel), while the westward-propagating components are defined to have negative wavenumber (i.e., on the left).

Looking at the spectra in Fig. 3 then, we see that like in Fig. 2, the spectra are quite red, but this time in both frequency and wavenumber. That is, the power is concentrated around planetary zonal wavenumber-0 (i.e. the zonal mean) and the lowest frequencies. The absolute spectral peak anywhere in the domain, however, is at around eastward wavenumbers 1 to 2, and periods between 30 and 90 days (the lowest frequency displayed is 1/96 cpd). This spectral peak is for the MJO, the same phenomena that appeared in Fig. 2, and it can be seen to be present mostly in the symmetric component, but also somewhat in the antisymmetric component.

Also noticeable in the spectra are several 'ridges' in the contours. For example, in the antisymmetric component for westward propagating waves with periods around 4 to 6 days and wavenumbers 0 to −5.

a) LOG $\left\{ \sum_{15\,S}^{15\,N} \text{POWER(OLR A)} \right\}$

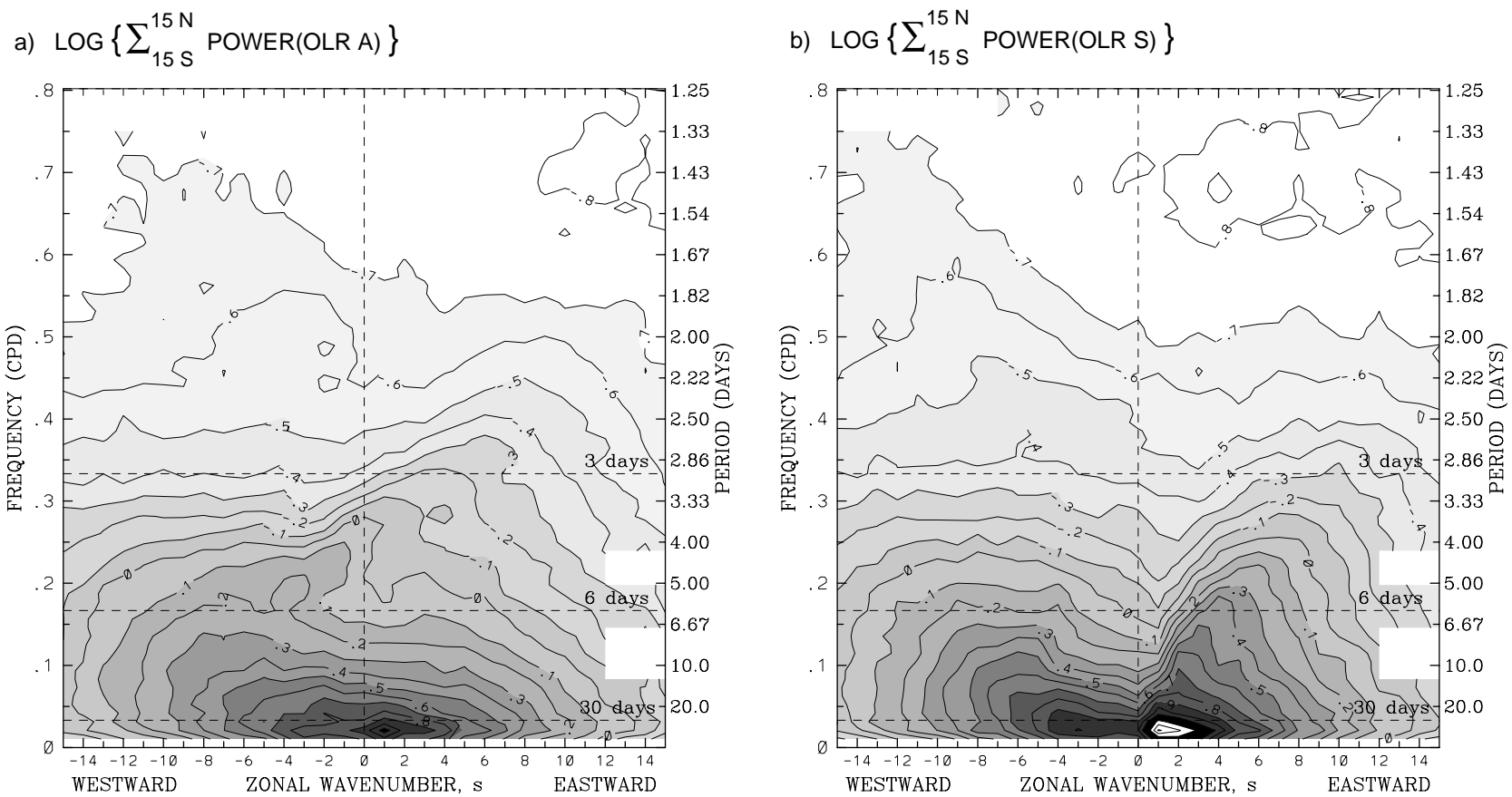b) LOG $\left\{ \sum_{15\,S}^{15\,N} \text{POWER(OLR S)} \right\}$

FIG. 3: Zonal wavenumber-frequency power spectra of the (a) antisymmetric component and (b) symmetric component of OLR, calculated for the period of record from 1979 to 1996 using twice-daily observations. The power was calculated independently at each latitude (on a 2.5° grid) and then summed over 15°S to 15°N. The base-10 logarithm was applied for the convenience of plotting. Contour interval is 0.1 arbitrary units. Shading is incremented in steps of 0.2. Certain erroneous spectral peaks from artifacts of the satellite sampling (eastward wavenumber 14 and periods of 9 and 4.5 days) are not plotted. More details are in Wheeler and Kiladis (1999).
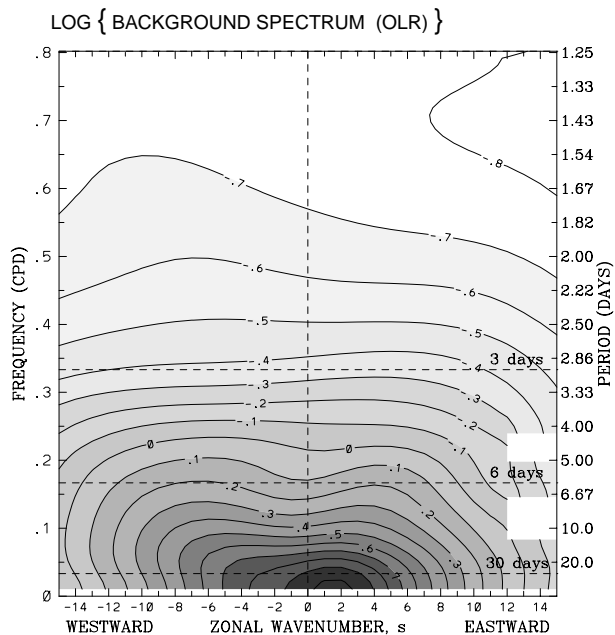
LOG { BACKGROUND SPECTRUM (OLR) }

FIG. 4: Zonal wavenumber-frequency spectrum of the base-10 logarithm of the "background" power calculated by averaging the individual power spectra of Figs. 3a and 3b, and smoothing many times with a 1-2-1 filter in both wavenumber and frequency. The contour interval and shading are the same as in Fig. 3 (taken from Wheeler and Kiladis 1999).

These ridges are each an indication that there is more power acting at these scales than for the surrounding scales. In fact, it turns out that many of the ridges are statistically-significant spectral peaks when compared to a red-noise background spectrum. Such a red-noise background spectrum is displayed in Fig. 4, where this spectrum was simply constructed as a smoothed version of the original spectra.

Taking the ratio of the original spectral power (Fig. 3) with the background (Fig. 4) gives the contours displayed in Fig. 5. With shading, the statistically significant spectral peaks are highlighted, and we now see a variety of spectral peaks which can each be associated with a particular tropical wave.

c. *Identifying the tropical waves*

Given the spectral peaks of Fig. 5, we may identify the following tropical waves.

First, we have the MJO at low eastward-propagating wavenumbers and low frequencies (about 30 to 60 days), as already discussed. Of note here is that its spectral peak is proportionally greater than the background than any of the others (i.e. its ratio in Fig. 5 is generally greater than 2.0, something that is unfortunately ob-

scured by the tightly packed contours around the MJO peak).

Second, we have a number of spectral peaks that can be associated with theoretical equatorial waves. These are the spectral peaks that lie along the theoretical 'dispersion' curves that are also plotted. Ignoring for the moment where such curves come from, we see that they can be used to define a number of equatorial waves in the observations, and since they imply a coupling between the convection and the dynamics, they are called the "convectively coupled equatorial waves". They are the Kelvin wave, $n = 1$ equatorial Rossby (ER) wave, and $n = 1$ westward inertio-gravity (WIG) wave in the symmetric component of the OLR, and the mixed Rossby-gravity (MRG) wave, $n = 0$ eastward inertio-gravity (EIG) wave, and $n = 2$ WIG wave in the antisymmetric component. Other theoretical equatorial waves are curiously absent from the spectra, for example, $n \geq 2$ equatorial Rossby waves and $n \geq 1$ EIG waves.[1] The MJO, being away from any of the dispersion curves, is evidently unlike the convectively coupled equatorial waves.

Third, there is an indication of enhanced variance (relative to the background) in both the antisymmetric and symmetric components for synoptic-scale (planetary zonal wavenumber, $s \geq 6$) westward-propagating waves with periods between 3 and 6 days. This region of enhanced variance is associated with the disturbances that are observed within the intertropical convergence zones (ITCZs), and which have been variably called "easterly waves"[2] and "tropical-depression" (TD) -type disturbances. They often exist in the convection on one side of the equator only, hence their appearance in both the antisymmetric and symmetric components. This, together with their variable period and spatial structure from one region to the next, makes them the most difficult of the tropical waves to define by this spectral analysis, as is evident by their diffuse, and weak, spectral peak. For this reason, the rest of this paper concentrates less on the classic easterly waves than the

---

[1] Note that the $n = 2$ Rossby wave would be antisymmetric in this field, and the $n = 3$ symmetric. See also Section 5.

[2] The term "easterly wave" has been used rather loosely in the historical research literature such that almost any large-scale tropical disturbance observed moving toward the west (i.e. a wave in the trade-wind easterlies) has at times been given that name, including some of the disturbances that may be better categorized as equatorial waves. Most notably, the convectively coupled mixed Rossby-gravity waves have often been wrongly identified as easterly waves. I prefer to use the term easterly wave only for those disturbances that have no apparent link with an equatorially-trapped wave. When defined in this manner, the dynamics of easterly waves resembles that of a (non-equatorially-trapped) Rossby wave (e.g. Sobel and Horinouchi 2000).
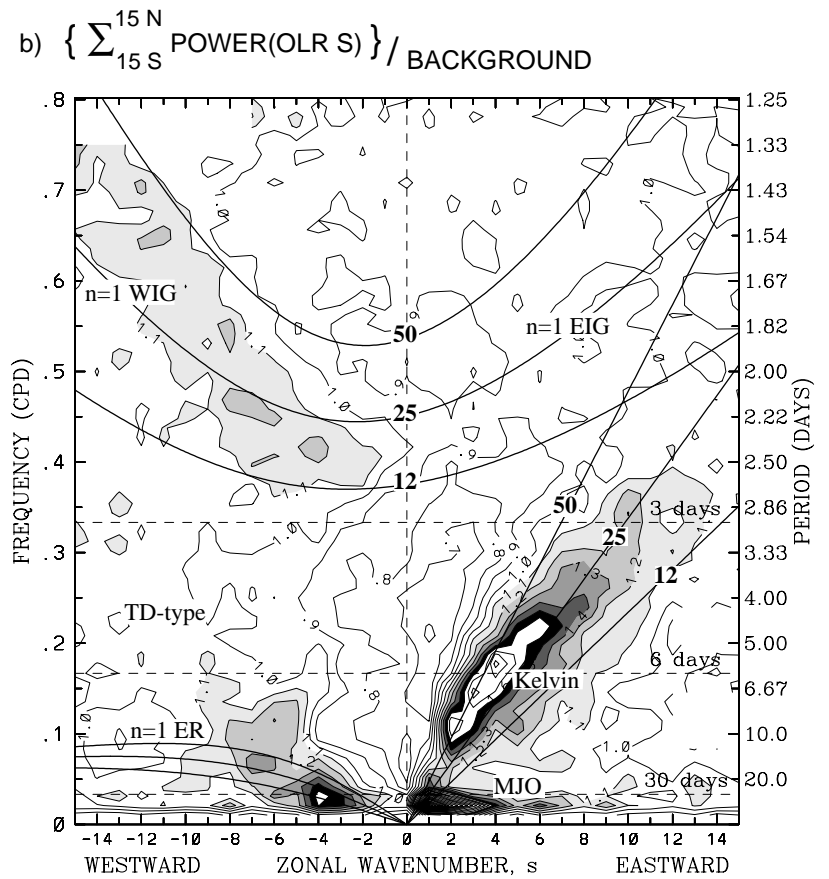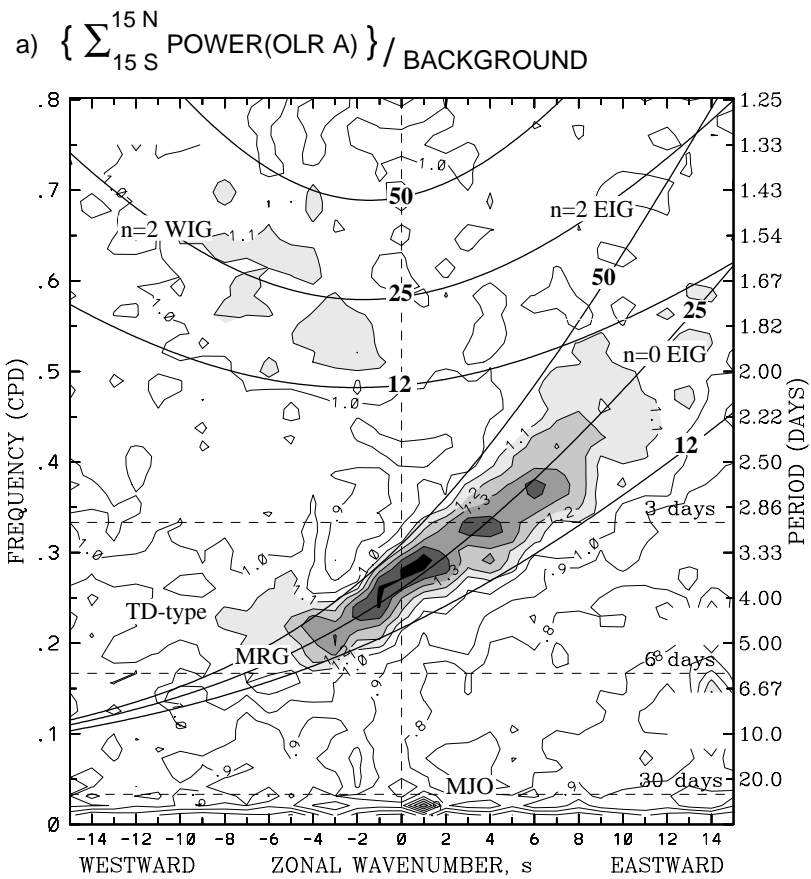
FIG. 5: (a) The antisymmetric OLR power of Fig. 3a divided by the background power of Fig. 4. Contour interval is 0.1, and shading begins at a value of 1.1 for which the spectral signatures are statistically significantly above the background at the 95% level (based on 500 dof). Superimposed are the dispersion curves of the even meridional mode-numbered equatorial waves for the three equivalent depths of $h = 12$, 25, and 50 m. (b) Same as in panel a except for the symmetric component of OLR of Fig.3b and the corresponding odd meridional mode-numbered equatorial waves (taken from Wheeler and Kiladis 1999).
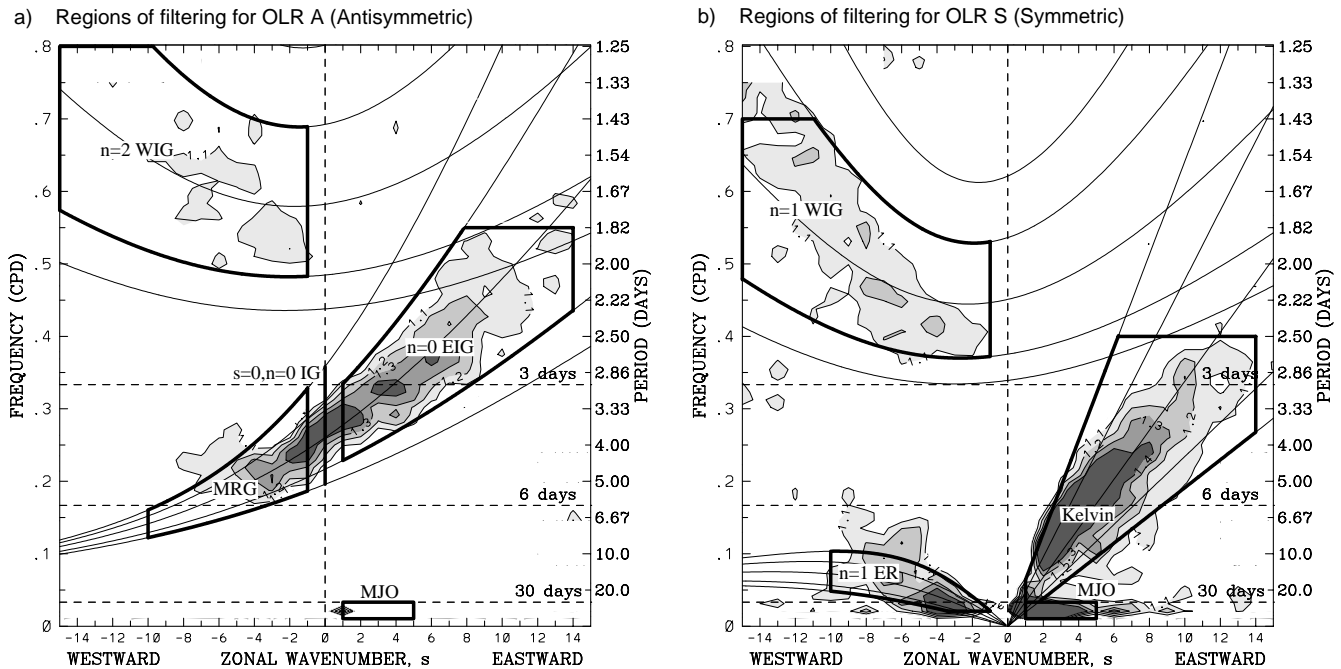
a) $\left\{ \sum_{15\,S}^{15\,N} \text{POWER(OLR A)} \right\} \Big/ \text{BACKGROUND}$

b) $\left\{ \sum_{15\,S}^{15\,N} \text{POWER(OLR S)} \right\} \Big/ \text{BACKGROUND}$

Fig. 6: Regions of wavenumber-frequency filtering (thick boxes) used to extract the various tropical waves (excluding 'easterly waves') from the OLR dataset for the (a) antisymmetric component and (b) symmetric component of the OLR. The box outlines are drawn such that they are inclusive, meaning that the wavenumber or frequency along which the thick line is drawn is included. Also shown are various equatorial wave dispersion curves for the equivalent depths of $h = 8$, 12, 25, 50, and 90 m (taken from Wheeler and Kiladis 1999).

other classes of tropical zonally-propagating waves.

3. Diagnostic wavenumber-frequency filtering

The characteristics of the various tropical waves may be studied further through the use of filtering. Filtering is a commonly used diagnostic tool in research as it can extract the variability acting on different time and/or space scales from a meteorological dataset. Its use by forecasters, on the other hand, is comparatively rare, the reason being that standard methods of frequency filtering require information for times beyond the time of interest, something that can not be obtained for real-time analysis. In this section we use filtering to look at the characteristics of past events of tropical waves, that is, what I call diagnostic filtering. Examples of filtering applied in a real-time situation will be given later in Section 7.

When filtering one must first define the frequencies and/or wavenumbers that one would like to extract. For the best-defined tropical waves, that is, the ones appearing as strong spectral peaks, we define the re-

gions as presented as the boxes in Fig. 6. Note that the MJO is defined to include both antisymmetric and symmetric components while the convectively coupled equatorial waves are defined to be either in one component or the other only.

While there are a variety of ways to perform filtering, here we use forward and inverse Fourier transforms, retaining only those spectral coefficients of the boxed regions before the inverse transforms. The technique is best shown through examples.

a. Example time-longitude realizations

Fig. 7 shows a section of unfiltered daily-averaged OLR for the period November 1987 to April 1988. For the convenience of viewing, anomalies with respect to the mean annual cycle are shown. The blue and purple shades are representative of enhanced convection and rainfall while the orange shading is representative of suppressed. A number of cases of eastward propagating anomalies at various scales can be discerned.

Fig. 8 shows filtered fields for the MJO and convectively coupled Kelvin wave for the same period as Fig. 7. Comparing the figures, one can identify most of the
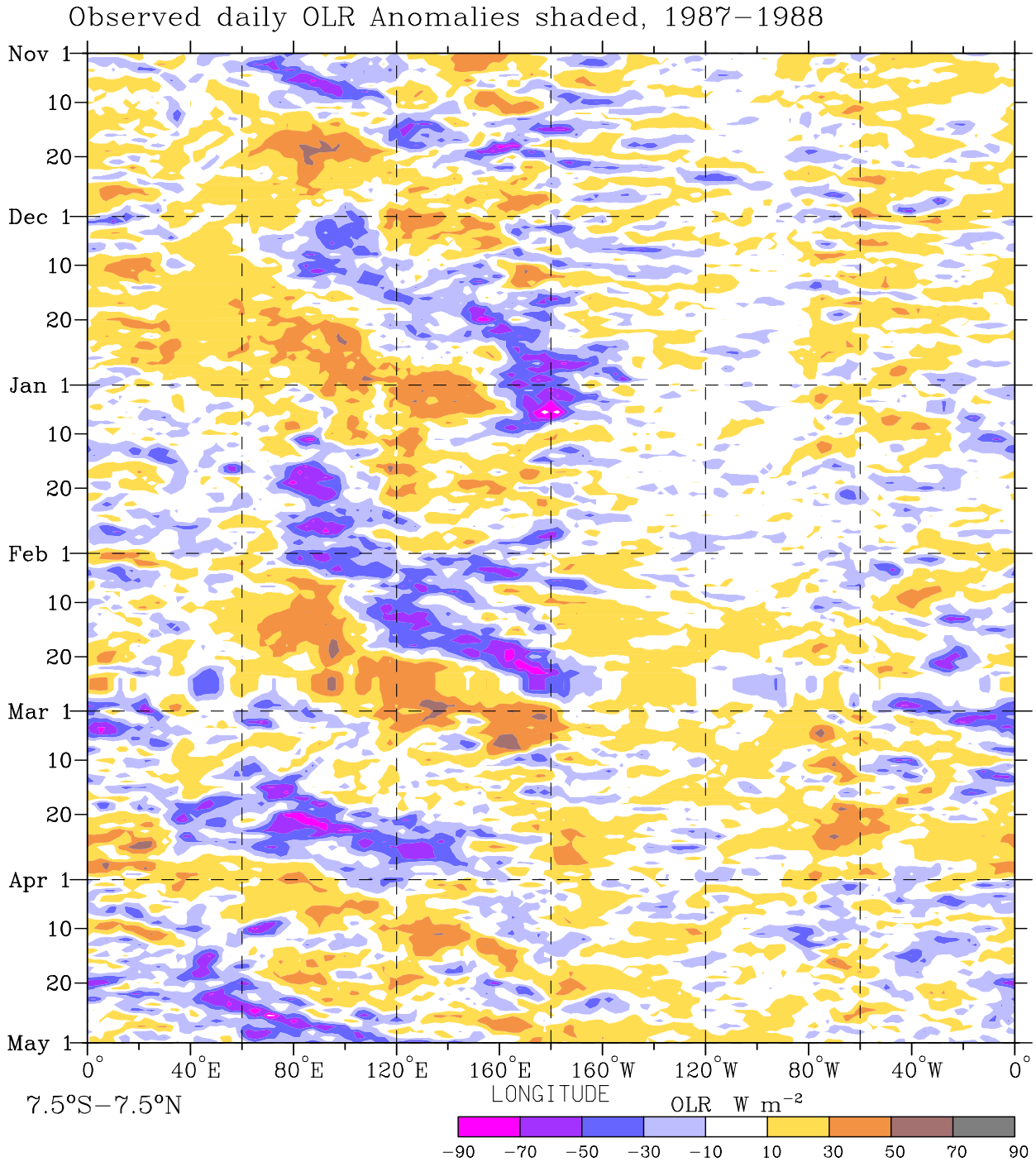
FIG. 7: Time-longitude section of daily OLR anomalies averaged for the latitudes from 7.5°S to 7.5°N. The anomalies are calculated by removing the long-term mean and the first 3 harmonics of the annual cycle at each grid-point.

eastward-propagating anomalies in the unfiltered field with either of these two types of tropical waves. The MJO events have a period around 1.5 months and are slowly propagating eastwards, while the Kelvin waves are faster propagating, and with a higher frequency. Both of these tropical wave types are an important influence for the weather in this latitude band during this period. At other times and for other latitudes, however, other tropical waves may dominate. For example, the off-equatorial section of Fig.1 is likely dominated mostly by a combination of MRG waves, ER waves, and easterly (or equivalently TD-type) waves.
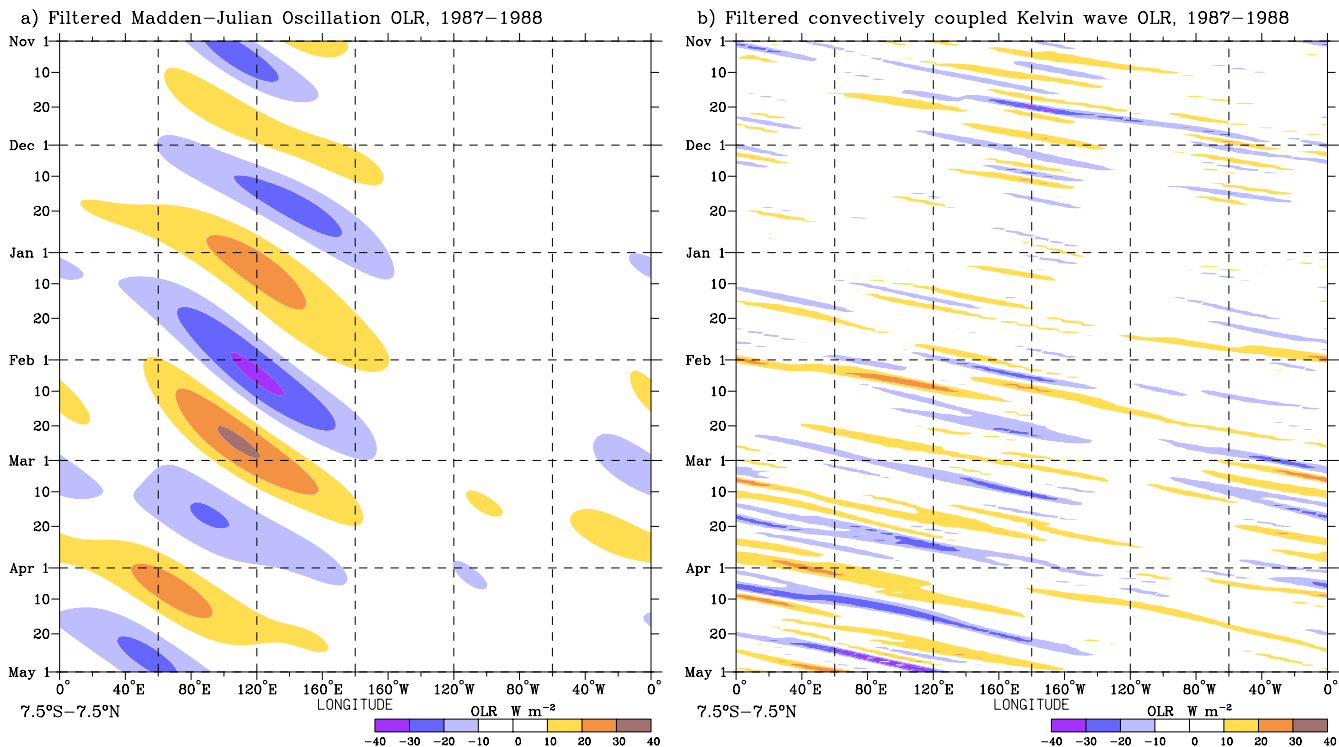
a) Filtered Madden–Julian Oscillation OLR, 1987–1988

b) Filtered convectively coupled Kelvin wave OLR, 1987–1988

FIG. 8: As in Fig. 7 except for sections of (diagnostically) filtered OLR anomalies for (a) the MJO and (b) the convectively coupled Kelvin wave.

b.   Geographical distributions of the filtered OLR variability

Other characteristics of the tropical waves that may be studied by filtering are their typical locations of occurrence. Filtering the whole OLR dataset (~ 20 years worth), one may calculate the standard deviation of each of the filtered fields at each grid-point, and plot it as a map.

Fig. 9 shows such maps for the MJO filtering, separately for southern summer (defined as November through April) and northern summer (May through October). In terms of moist convection, for which OLR is a good proxy, the MJO can be seen to be most active around the latitudes of about the equator to 15°S in southern summer, and at latitudes north of the equator in northern summer. Further, the longitudinal extent of the MJO convection can be seen to be restricted mostly to the Indian and western Pacific ocean regions.

Fig. 10 displays the same quantity except for the $n = 1$ ER wave. Compared to Fig. 9, it is notable that the displayed maps for the ER wave are symmetric about the equator. This is because we define the ER wave as being in the symmetric component of the OLR (i.e., OLRS) only, as indicated in Fig. 6. Also in comparison to Fig. 9, one can see that the standard deviations for the ER wave are in general less than those for the

MJO, thus the ER waves explain less of the convective 'weather'.

Turning now to the geographical distribution of the standard deviation of the Kelvin wave OLR (Fig. 11), we see that it is typically much more concentrated near the equator, and has a more global extent than the other waves, extending even into the Atlantic. Indeed, this distribution of the standard deviation appears quite consistent with the snapshot of the total record provided in Fig. 8b.

Further, the geographical distribution of the MRG wave variability is displayed in Fig. 12. This tropical wave is most active during northern fall, so we display its standard deviation for this portion of the year only. Of note is that this type of wave tends to be most active in a region around the date line, yet it can be observed almost anywhere across the Indian and Pacific ocean sectors as well, influencing convection primarily at off-equatorial latitudes from about 5 to 10°.

4.   'Conceptual models'

A conceptual model of a meteorological phenomenon is defined as an attempt to specify the idealized or generalized space distribution of meteorological elements
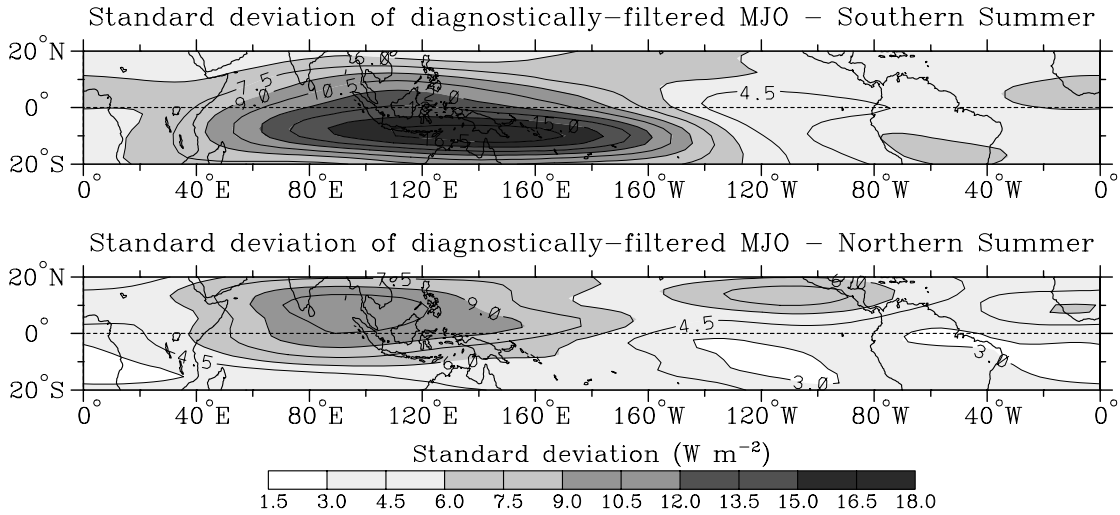
FIG. 9: Standard deviation of the diagnostically-filtered MJO OLR for the 10-year period of 1985 to 1994, separately for southern summer (above) and northern summer (below) (taken from Wheeler and Weickmann 2001).
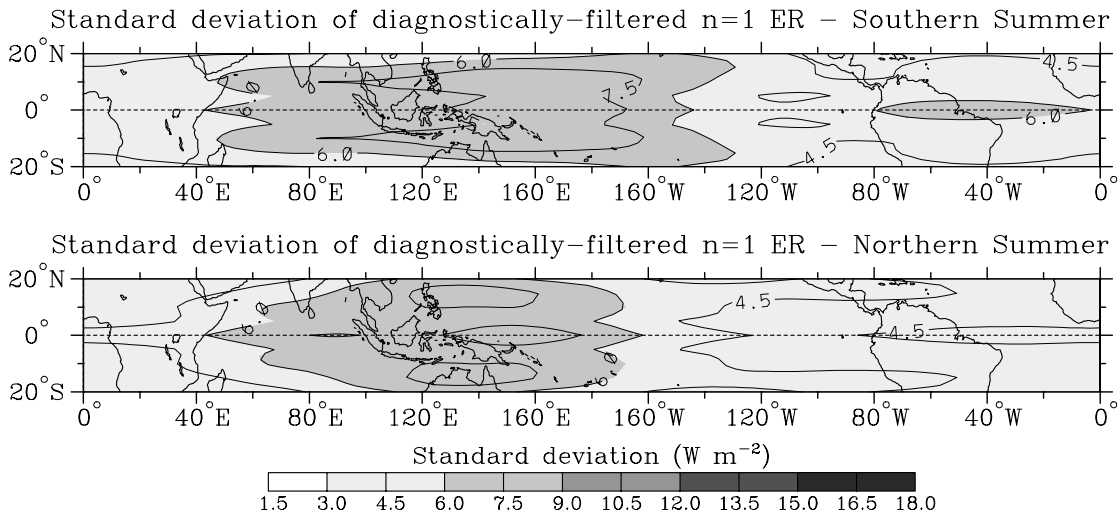

FIG. 10: As in Fig. 9 except for the convectively coupled $n = 1$ equatorial Rossby (ER) wave (taken from Wheeler and Weickmann 2001).

such as clouds, rainfall, wind, temperature or pressure in that distinct type of atmospheric system. Here we briefly look at some of the conceptual models that have been produced for the lower-frequency tropical waves. Often, spectral analysis and filtering of the historical datasets is used in the process of producing such conceptual models.

a. Madden-Julian oscillation

This is the most well-known of the tropical waves, and its most well known conceptual model is reproduced in Fig. 13. This figure is a schematic based on the evidenced amassed by Madden and Julian from com-

positing a number of MJO events during an 18-month period (during 1957–1958). It gives an indication of the vertical structure of the wave along the equator. Of note is the fact that the schematic indicates that the convection associated with the MJO is limited to the Indian to western Pacific Ocean regions, while the (anomalous) circulation associated with the MJO has a more global extent. Over the Indian to western Pacific sectors the circulation is 'coupled' to the convection, while elsewhere the circulation is essentially 'dry', that is, without convection. Also, the dry vertical circulation component over the central to eastern Pacific propagates more quickly to the east than the convective component over the warmer waters of the western Pa-
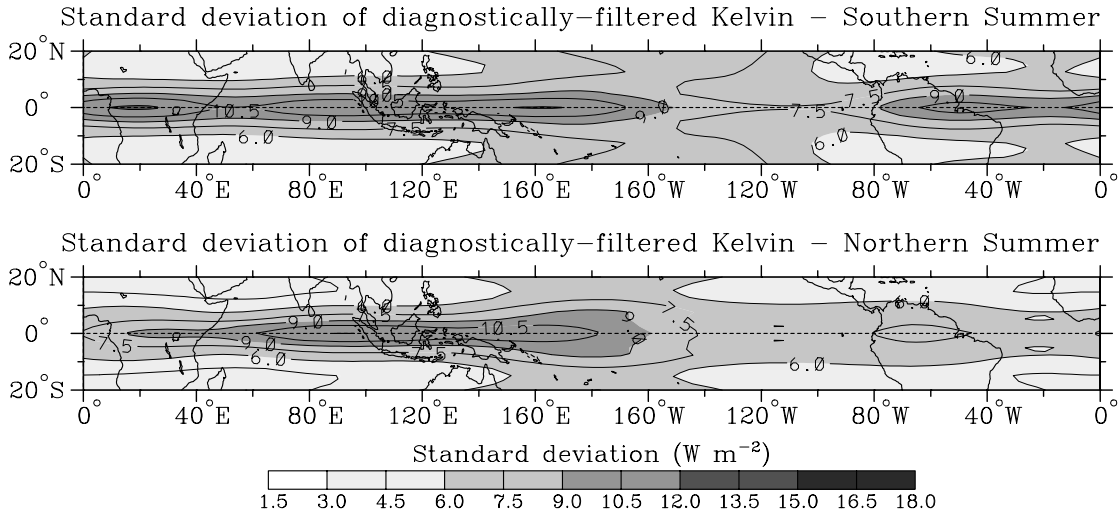
Standard deviation of diagnostically–filtered Kelvin – Southern Summer

Standard deviation of diagnostically–filtered Kelvin – Northern Summer

Standard deviation (W m^{-2})

FIG. 11: As in Fig. 9 except for the convectively coupled Kelvin wave (taken from Wheeler and Weickmann 2001).

Standard deviation of diagnostically–filtered MRG – Northern Fall
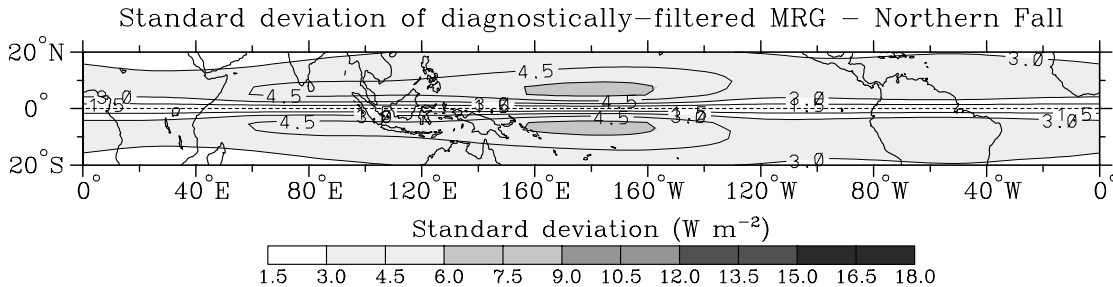
Standard deviation (W m^{-2})

FIG. 12: As in Fig. 9 except for the convectively coupled mixed Rossby-gravity (MRG) wave, and for the season of northern fall (defined as August to January) only (taken from Wheeler and Weickmann 2001).

cific. The speed of propagation of the latter is about 5 m s^{-1}, consistent with that obtained from the filtering of OLR for a sequence of cases in Fig. 8a.

What the schematic of Fig. 13 doesn't show about the MJO, however, is its typical horizontal structure. A useful conceptual model of this is as presented in the schematic of upper-tropospheric circulation for the MJO in Fig. 14. This schematic was constructed based on spectral and cross-spectral analysis of many years of data. An important feature of this circulation is that it has the appearance of what is commonly known as the Gill pattern, after Gill (1980), with off-equatorial circulation cells of a forced equatorial Rossby wave to the west of the "cloud" region and equatorial zonal flow of a Kelvin wave to the east.[3] Of course, to identify such circulation patterns in an operational forecaster's synoptic chart would be quite difficult, as not only would this pattern of flow be superimposed upon the mean winds (e.g. those of the mean Walker and Hadley circu-

lation cells), but it would be superimposed upon variability acting on other time scales as well (e.g. tropical cyclones and other tropical waves).

b. *Convectively coupled n = 1 equatorial Rossby wave*

A conceptual model of a convectively coupled $n = 1$ ER wave is provided in Fig. 15. Shown are horizontal maps of anomalous OLR, 850 hPa streamfunction, and 850 hPa winds calculated from observations using a regression technique. The regressions were computed at various lags against an index of the ER waves constructed by filtering. This 'typical' convectively coupled ER wave can be seen to consist of anomalous circulation cells on both sides of the equator slowly moving to the west with new circulation cells developing to their east. The propagation (phase) speed of these features is around 5 m s^{-1} to the west. The negative anomalous OLR, and hence enhanced convection, tends to be in the regions of anomalous low-level poleward and/or westerly flow. Such a structure for the ER wave is usu-

---

[3]For a brief discussion of the essential theoretical characteristics of equatorial Kelvin and Rossby waves, refer to Section 5.
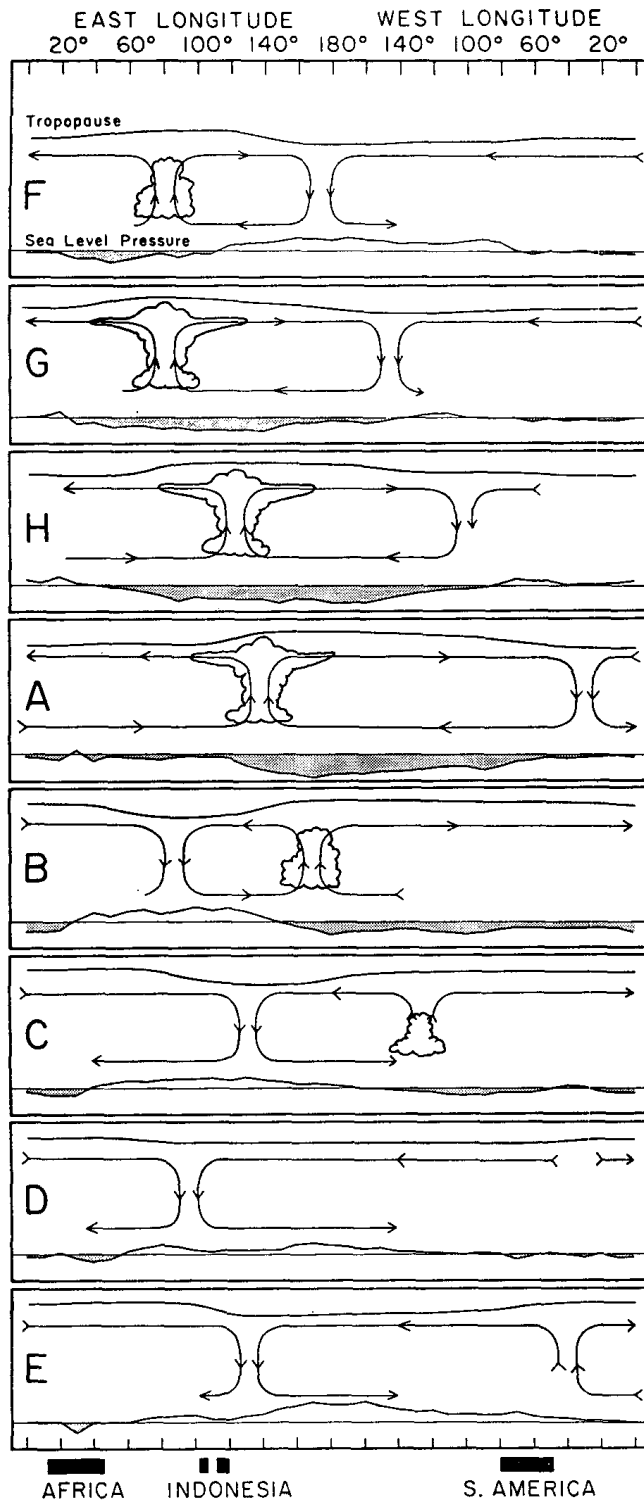
FIG. 13: Schematic depiction of the time and space (zonal plane) variations of the Madden-Julian oscillation. Dates are indicated symbolically by the letters at the left of each chart and each panel is separated by approximately 5–6 days. The pressure of the disturbance is plotted at the bottom of each chart with negative anomalies shaded. The circulation cells are based on the zonal winds, with the vertical motion coming from what may be inferred from continuity considerations and observations of humidity. Inferred regions of enhanced large-scale convection are sketched as clouds. The relative tropopause height is indicated at the top of each chart (taken from Madden and Julian 1972).
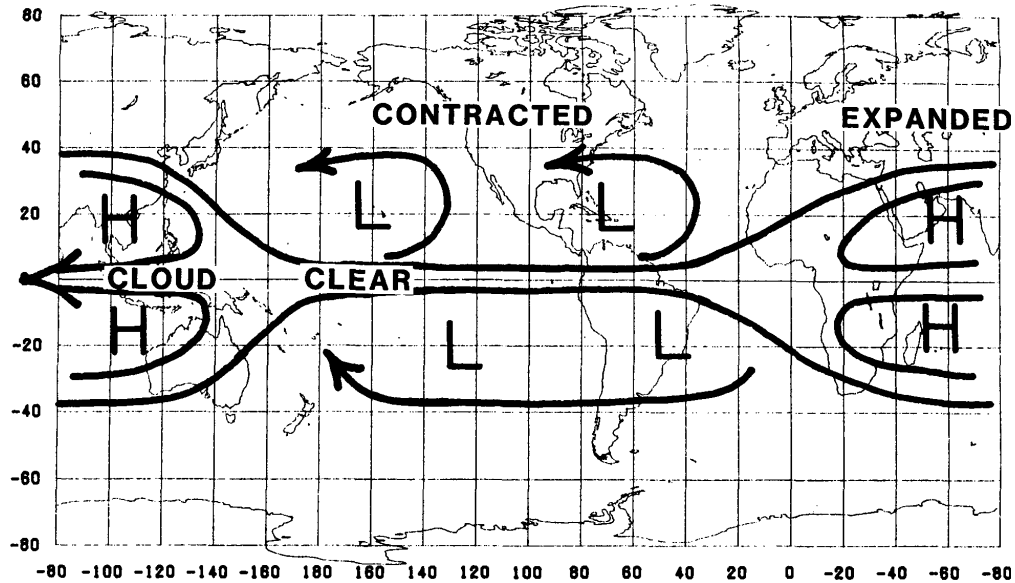
FIG. 14: Schematic of the relationship between convection, as signified by "cloud" and "clear" regions, and the 250-hPa circulation for the MJO at a time when maximum cloudiness is over the Indonesian region (taken from Weickmann et al. 1985).

ally best developed in the mid to lower-troposphere.

c. Convectively coupled Kelvin wave

Fig. 16 presents the typical horizontal structure of a convectively coupled Kelvin wave, as also calculated from regression analysis. It shows the upper-tropospheric flow and geopotential associated with the wave, together with the OLR. Like for the MJO, the region of enhanced convection propagates to the east with the wave, although at a much faster rate (about 15 m s^{-1}). The convection is also more concentrated at the equator than what is observed for the MJO, with a smaller meridional extent. The flow is also mostly zonal, without the Rossby gyres of the Gill-pattern of the MJO (cf. Fig. 14). Evidently, this is another distinct mode of the tropical atmosphere that deserves its own conceptual model. In some of the research literature it has been called a "supercluster" or "super cloud cluster". Further, like all of the tropical waves it may occur either in conjunction with other waves or independently. Only during times when it is acting independently is it likely to be seen in a standard synoptic analysis chart as typical wind anomalies are only on the order of 2 m s^{-1}.

d. Convectively coupled mixed Rossby-gravity wave

Another useful conceptual model is provided in Fig. 17. It presents the typical lower-tropospheric structure of a convectively coupled MRG wave. Like in the conceptual model figures for the other tropical waves, this plot shows anomaly fields only. In the anomalies, the MRG wave presents itself as circulation cells centred on the equator (moving to the west) with enhanced convection mostly in regions of low-level poleward flow. If one was to superimpose the anomaly fields upon the mean easterlies that occur in this region, however, the result would look somewhat different. Instead of distinct circulation cells, the strength of the mean winds may be such that the wave appears as a north-south meandering in the easterly streamlines only. Importantly, such meandering streamlines, or 'troughs' and 'ridges' in the easterlies, are predominantly antisymmetric across the equator for the MRG wave. This is the primary distinction between this wave and what is best defined as an easterly wave, as shown next.

e. Easterly waves or tropical depression-type disturbances

The horizontal structure of a typical easterly wave of the northwestern Pacific is shown in Fig. 18. As has already been mentioned, this wave typically shows perturbations on one side of the equator only. It also has quite a strong signature in the vorticity field. As such, it has been found by researchers that many aspects of their dynamics can be explained by barotropic Rossby wave theory, that is, non-equatorially-trapped Rossby waves. Enhanced convection is typically in the region of the cyclonic vorticity and/or poleward flow. If a trough axis was drawn, this region of enhanced convection would

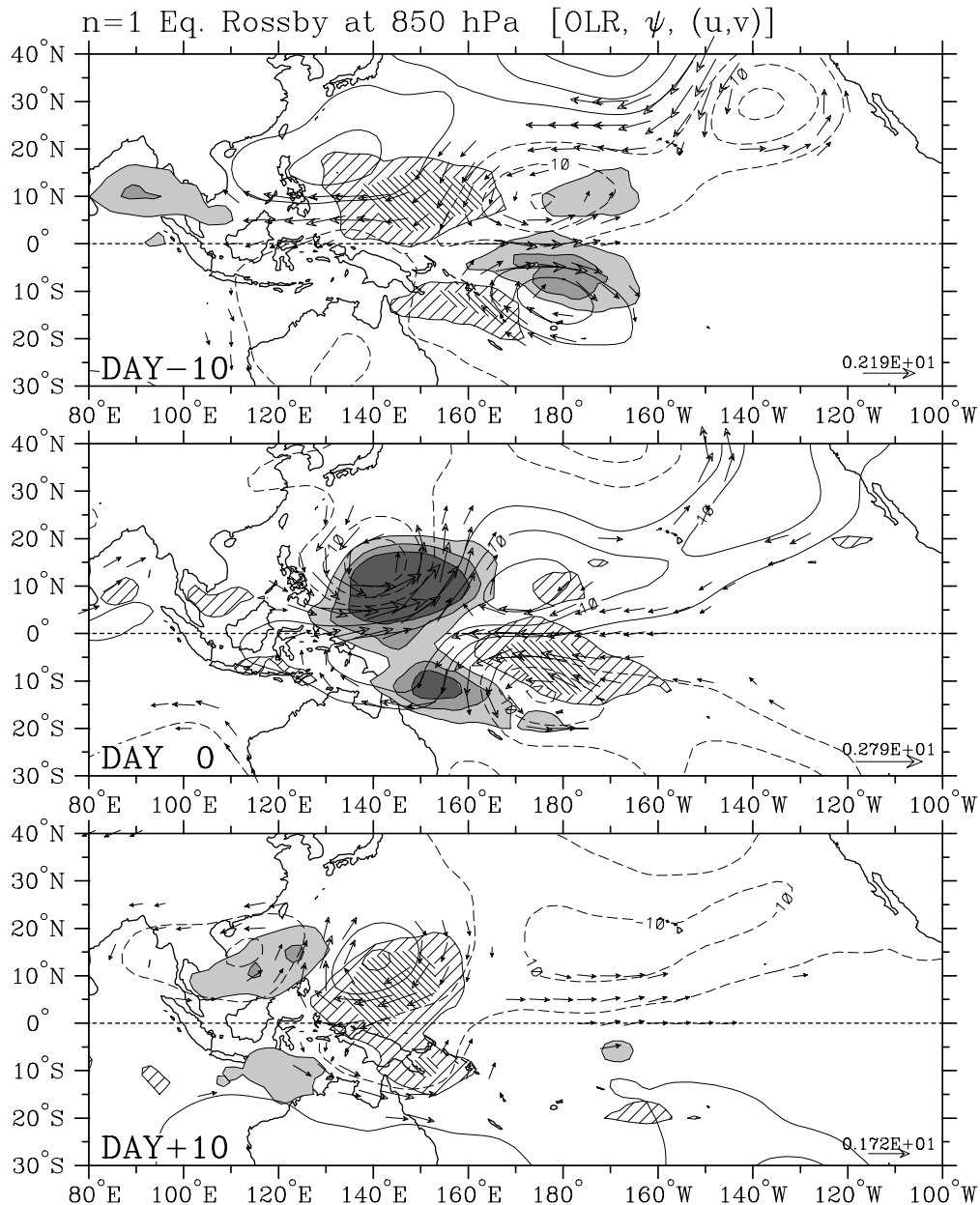## n=1 Eq. Rossby at 850 hPa [OLR, ψ, (u,v)]

FIG. 15: Typical horizontal structure of anomalies associated with a convectively coupled $n = 1$ equatorial Rossby wave over a sequence spanning 21 days, as calculated using regression analysis. Shading/cross-hatching show the negative/positive OLR anomalies, indicating enhanced/suppressed convection. Contours are streamfunction anomalies at the 850 hPa level, indicating the lower-level rotational winds. Vectors are the 850-hPa wind anomalies of the wave (taken from Wheeler et al. 2000).

be near and to the east of the trough axis. Although difficult to consistently define, they appear to be common in both the Pacific and Atlantic regions, generally north of the equator. Like the MRG and ER waves, they propagate to the west.

5. Some discussion of theory

As can be discerned from the preceding discussion, many of the features of the tropical waves can be well described and understood by some rather simple theory, that is, the theory of equatorially-trapped waves. It is thus useful to have some understanding of this theory. Here, I will mostly describe the concepts of the theory in words. For a more complete development refer to sections 11.4 of the texts of Gill (1982) or Holton (1992).

The theory may start with what are known as the primitive equations, that is, the full set of basic equations that governs the time evolution of the three-dimensional large-scale motion field in the (dry) stratified atmosphere. These equations are often written as
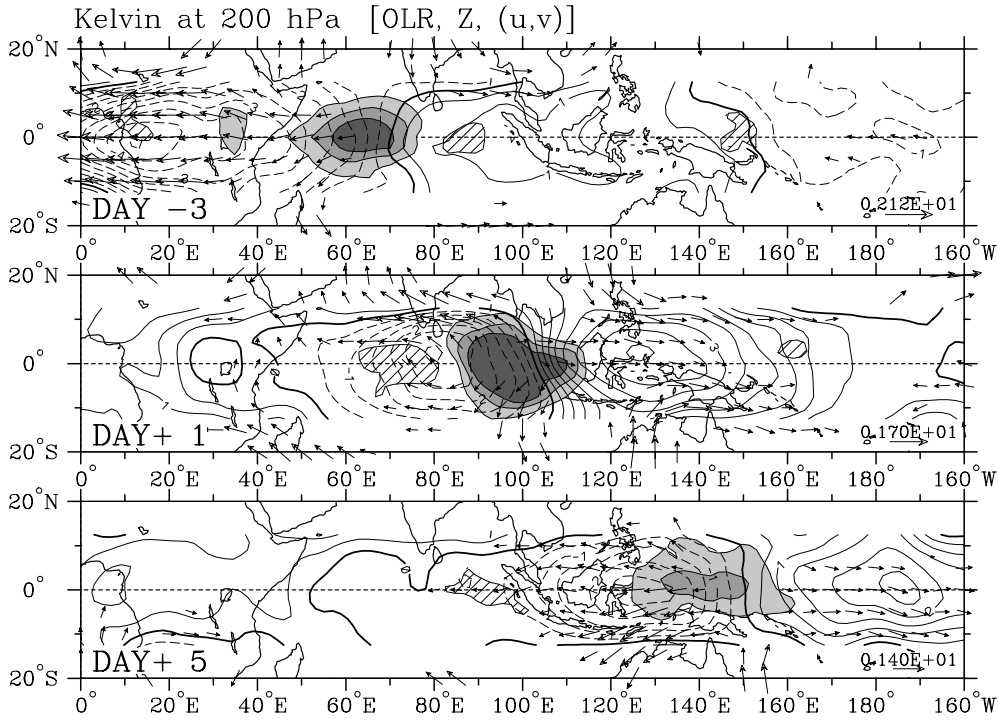
FIG. 16: Typical horizontal structure of anomalies associated with a convectively coupled Kelvin wave over a sequence spanning 9 days, as calculated using regression analysis. Shading/cross-hatching show the negative/positive OLR anomalies, indicating enhanced/suppressed convection. Contours are geopotential height anomalies at the 200 hPa level. Vectors are the 200-hPa wind anomalies of the wave (taken from Wheeler et al. 2000).
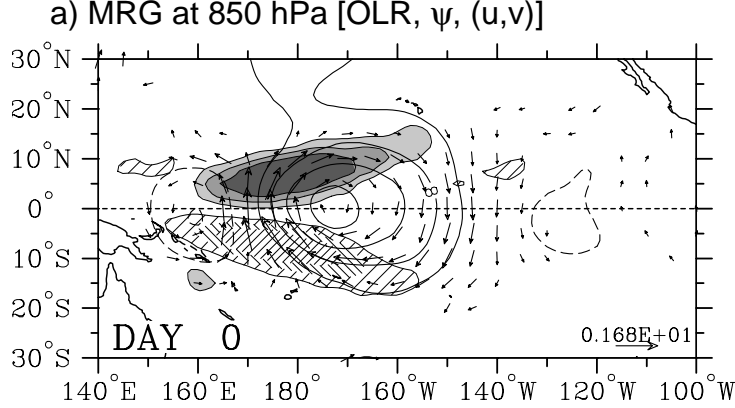

FIG. 17: Typical horizontal structure of anomalies associated with a convectively coupled mixed Rossby-gravity wave, as calculated using regression analysis. The same fields are shown as in Fig. 15.

six equations in six unknowns: the zonal velocity, meridional velocity, vertical velocity, density, pressure, and temperature.

The full primitive equations are no doubt difficult to analyse. However, given certain assumptions (e.g. linearized equations about a basic state with no motion), the primitive equations may be separated into an infinite set of independent "shallow water" equations, and a vertical structure equation. The shallow water equa-

tions govern the horizontal and time-varying behaviour of the flow of each "normal mode", and are written as three equations in three unknowns only. They are evidently much simpler to analyse, and can be written for the equatorial region as

$$\frac{\partial u_l'}{\partial t} - \beta y v_l' = -\frac{\partial \Phi_l'}{\partial x} \qquad (1)$$

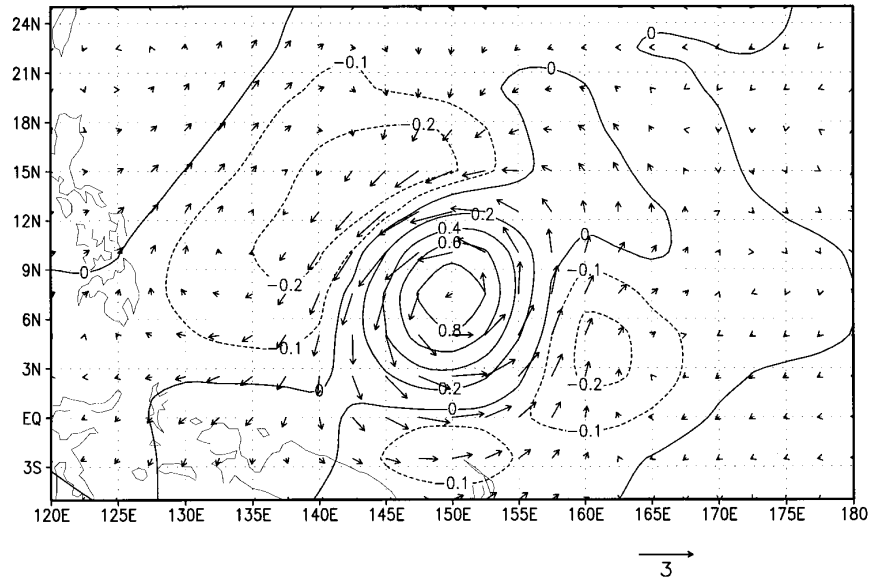$$\frac{\partial v_l'}{\partial t} + \beta y u_l' = -\frac{\partial \Phi_l'}{\partial y} \qquad (2)$$

FIG. 18: Typical horizontal structure of anomalies associated with an "easterly wave" or "tropical-depression" (TD)-type disturbance in the northwest Pacific, as calculated using regression analysis. Shown are 850-hPa winds (m s^{-1}) and 850-hPa vorticity (10^{-5} s^{-1}) (taken from Sobel and Bretherton 1999).

$$\frac{\partial \Phi_l'}{\partial t} + g h_l \left(\frac{\partial u_l'}{\partial x} + \frac{\partial v_l'}{\partial y} \right) = 0 \qquad (3)$$

where β is the equatorial value of the β-parameter ($\beta \equiv \partial f / \partial y$), g is the acceleration due to gravity, h_l is the equivalent depth, u_l' and v_l' are the (horizontal) velocities in the x and y directions respectively, and Φ_l' is the geopotential. Of note is that we have applied what is known as the equatorial β-plane approximation here, where the Coriolis parameter f is replaced by the linear function βy, where β is assumed to be constant. Further, the primes denote the fact that these are perturbation fields relative to the basic state of no motion about which the equations are linearized, while the l signifies that these equations govern a particular vertical normal mode only. In the shallow water equations, the unknown variables are a function of horizontal position (x, y) and time (t) only.

Note that although these equations as written are equivalent to those for perturbations to the free surface of a shallow layer of incompressible, homogeneous density fluid of mean depth h_l (also called the divergent barotropic model), these equations are equally valid for internal modes of motion of the stratified atmosphere provided the correct choice of h_l is made. Then, the full three-dimensional structure of the internal modes of motion is obtained by multiplying the shallow water solutions by an appropriate vertical structure function, that is, a function of height (z).

Without going into the details of the mathematical analysis, it is sufficient for this paper to say that

the "equatorial waves" are the valid wave-solutions of the shallow-water equations (1)–(3) in the vicinity of the equator. Everything that is needed to define their rather complicated structure and properties is included in these equations, and these characteristics can be neatly described by what are known as the dispersion relations of the waves (Fig. 19), and their horizontal structures (e.g., Fig. 20). Their existence relies crucially on the change in sign of the Coriolis force at the equator, as is contained in the term βy.

Looking at Fig. 19, we see the same curves that were used to define some of the tropical waves in Fig. 5. There are two main classes of waves, along with two additional waves. The two classes are the Rossby (or planetary) waves, which are westward propagating only, and the inertio-gravity waves, which can be either westward or eastward. Individual waves within these classes are denoted by a different integer value of n, where n is the meridional mode number. Waves of larger n have more complicated meridional structures. The two additional waves are the mixed Rossby-gravity wave and the Kelvin wave. The higher frequency waves tend to be more divergent in character, while the lower frequency waves are more rotational (and geostrophic).

The curves in Fig. 19 are drawn as functions of non-dimensionalized frequency and wavenumber. When drawn for dimensionalized units (as in Fig. 5), an important parameter for their value is the equivalent depth, h_l. For large-scale internal modes of motion in the troposphere, realistic equivalent depths may be anywhere
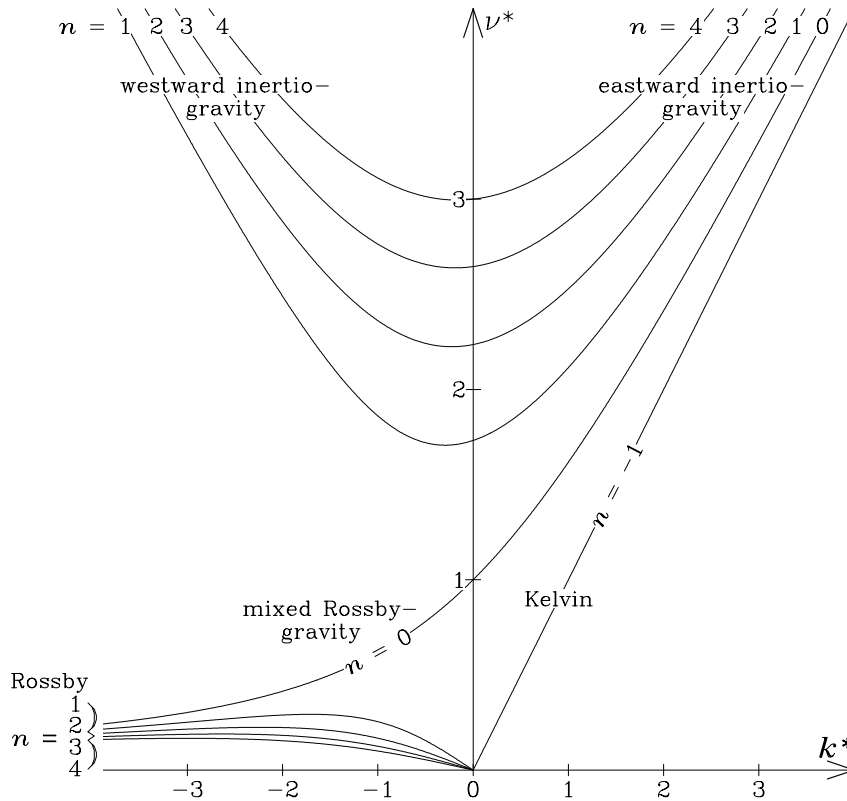
FIG. 19: Dispersion curves for equatorial waves (up to $n = 4$) as a function of the non-dimensional frequency, ν^*, and zonal wavenumber, k^*, where $\nu^* \equiv \nu/(\beta\sqrt{gh_l})^{1/2}$, and $k^* \equiv k(\sqrt{gh_l}/\beta)^{1/2}$ (as in Matsuno 1966). These dispersion relations ultimately come from the shallow water equations, (1)–(3). Eastward propagating waves (relative to the zero basic state employed) appear on the right, and westward propagating waves on the left.

in the range of about 10 to 300 m. As is indicated in Fig. 5, the convectively coupled equatorial waves occupy the lower end of this range. Equatorial waves that are not coupled to convection may exist for higher equivalent depths (~ 200 m). This serves to cause the convectively coupled waves to exist for lower frequencies than 'dry' waves of the same wavenumber. Equivalently, the convectively coupled waves move more slowly than the dry waves.

Another useful concept from the theory is that of phase speed and group velocity. Noting that the zonal phase speed is defined as $c_p \equiv \nu/k$, and the group velocity as $c_g \equiv \partial\nu/\partial k$ (see, for example, section 7.2 of Holton 1992), the different dispersion characteristics may be inferred from the curves of Fig. 19. That is, the group velocity is the local slope of the curves, while the phase speed is determined by the position on the diagram relative to the origin.

The group velocity determines how the energy of a 'packet' of each of the waves will disperse. Thus for a Kelvin wave, for which $\nu \propto k$, the group velocity is identical to the phase speed, and thus the wave is non-dispersive. This is consistent with the observations of Fig. 16 for which the energy and the phase propagate

together to the east. Conversely, the group velocity of an equatorial Rossby wave is near zero (the dispersion curves have near zero slope) hence the energy of the wave packet in Fig. 15 stays in much the same place, while an individual component (or phase) of the wave propagates through the wave packet to the west.

Fig. 20 displays horizontal structures for four of the more common equatorial waves. Many further consistencies can be seen between the theoretical waves and the observed convectively coupled equatorial waves. The MRG wave has circulation cells centred on the equator while the $n = 1$ ER wave consists of twin circulation cells on both sides of the equator. The Kelvin wave, on the other hand, consists of purely zonal flow. The regions of divergence and convergence of the theoretical waves, as indicated by shading, are also generally consistent with the regions of suppressed and enhanced convection of the observed equatorial waves, with the $n = 0$ waves being antisymmetric, and the $n = 1$ ER and Kelvin waves symmetric. In contrast, the easterly waves (Fig. 18) have horizontal structures that do not easily match any of the equatorial waves, while the MJO (Fig. 14) has a structure that combines components of both the Kelvin and $n = 1$ ER waves.
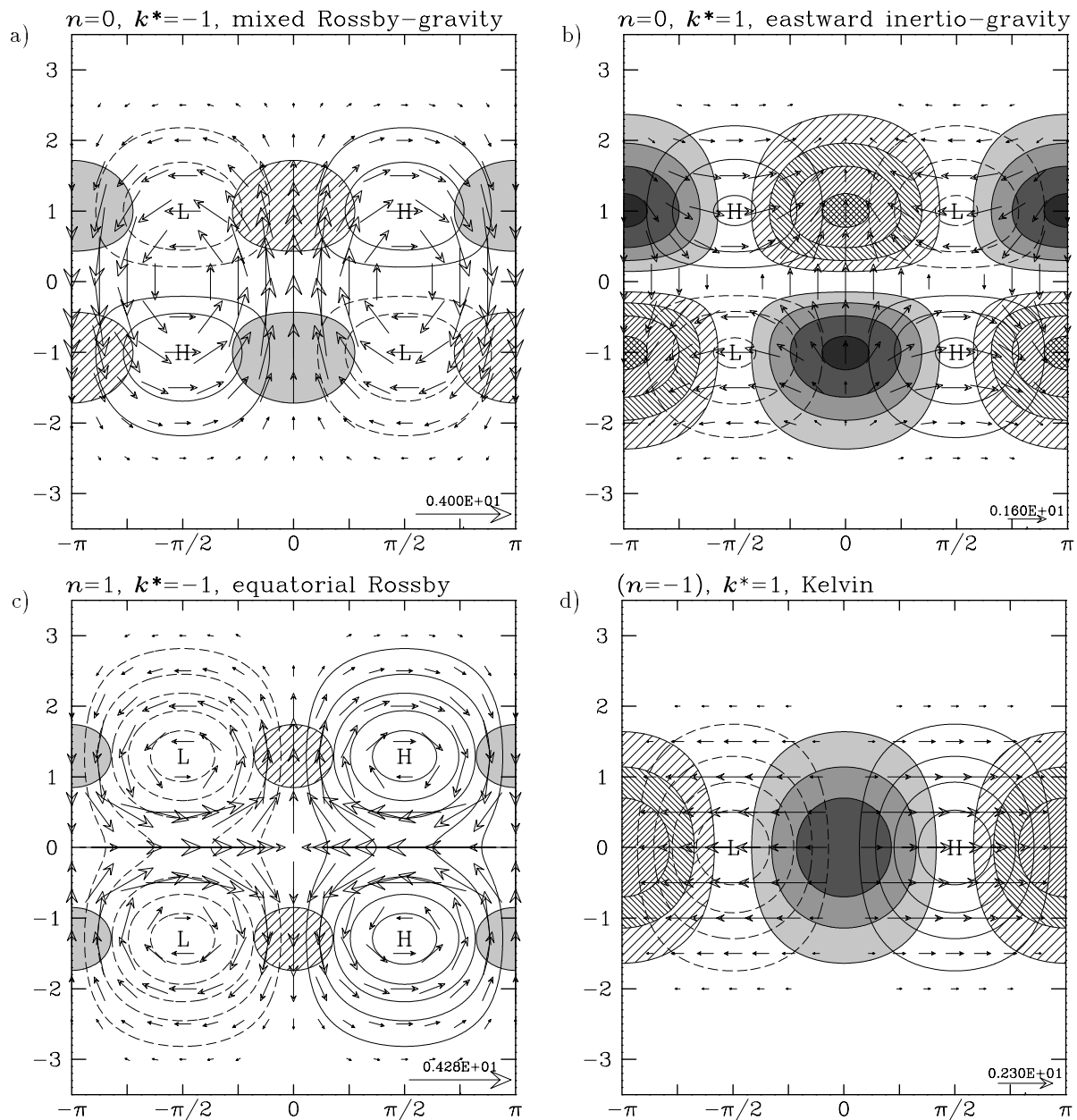
FIG. 20: Horizontal structures of the (a) mixed Rossby-gravity wave, (b) $n = 0$ eastward inertio-gravity wave, (c) $n = 1$ equatorial Rossby wave, and (d) Kelvin wave, each for non-dimensional zonal wavenumber $|k^*| = 1$. All scales and fields have been non-dimensionalized by taking the units of time and length as $[T] = (1/\beta\sqrt{gh_l})^{1/2}$, and $[L] = (\sqrt{gh_l}/\beta)^{1/2}$, respectively. The equator runs through the center of each diagram. Hatching is for convergence and shading for divergence, with a 0.6 unit interval between successive levels. Unshaded contours are for geopotential, with a contour interval of 0.5 units. Negative contours are dashed and the zero contour is omitted. The largest wind vectors are as specified in the bottom-right corner.

Finally, the above theory is strictly for dry waves, those without the influence of convection, only. For the observed tropical waves, interaction between the convection and dynamics is no doubt important, after-all, the latent heating of convection is one of the most important energy sources for atmospheric motions in the tropics. While many theories have been developed to attempt to account for such interaction, they are not as well accepted as that for the dry waves. In general, however, the theories all usually result with the conclusion that the moist, convectively coupled waves slow down relative to their dry counterparts.

6. Some discussion of forecasting

So far, this paper has concentrated on showing just the existence and characteristics of the tropical waves.

The value of the knowledge of their existence for forecasting has not yet been discussed.

It is first of note that each of the tropical waves explain only a fraction of the total variability of the convective weather. Even the MJO, which on the whole explains the most variance (Fig. 9), accounts for only on the order of 10% of the total OLR variance of all scales from diurnal up to seasonal on a 2.5° grid. Of course, the MJO would explain a greater portion of the variance of 5-day means, and a greater portion of the variance of a larger-scale average (e.g. a 10° latitude by 10° longitude average). Thus if forecasts of say the 5-day mean precipitation over a 10° box are considered to be useful, then predictions of the MJO would certainly be useful.

Despite their 'explanation' of less of the overall variance, benefit may also come from forecasts of the other tropical waves, especially considering that at times they are quite strong. For example, the convectively coupled Kelvin waves of Fig. 8b are noticeably stronger in the eastern hemisphere during March and April than during the preceding months. During times that a particular tropical wave disturbance is strong, it accounts for a greater portion of the total variance, and at these times certain benefit could come from forecasting them.

Also of note is that many of the various tropical waves have time scales that are quite relevant to atmospheric prediction, especially on the medium to longer range (i.e., greater than a few days, see Fig. 5), and this time scale is currently at or beyond the limit which can be skillfully forecast by numerical weather prediction (NWP) models in the tropics, especially with regards to convection or rainfall. An example of NWP forecasts of tropical precipitation in Fig. 21 illustrates this.

The far left panel of Fig. 21 shows precipitation rates derived from the satellite-borne microwave sounding units (MSU) for the period December 1987 through April 1988 averaged from 15°S to the equator. Three prominent enhanced convective phases of the MJO can be seen propagating to the east across the domain. The MJO has a fairly consistent period of about 1.5 months during this time.

The middle and right panels of Fig. 21 show how well this precipitation could have been forecast by a fairly modern (as of 1996) NWP model, specifically, the U.S. National Center for Environmental Prediction (NCEP) T62L28 Medium Range Forecast (MRF) model (Schemm *et al.* 1996). The 5-day forecasts show some evidence of the intraseasonal MJO variability, but the 15-day forecasts show no evidence of the variability at all. Clearly, a subjective forecast based on the knowledge of the existence of the MJO could have provided

more skill at this time. In general, current subjective or empirical predictions of the MJO and other longer time-scale tropical waves can provide a better medium to longer-range forecast than a NWP model. The next section presents such an empirical forecasting technique.

7. Real time wavenumber-frequency filtering

One of the major difficulties for using the large-scale tropical waves for forecasting is being able to identify their existence and location in real time. Unlike what can be done in diagnostic studies of tropical waves (e.g., Section 3), standard methods of low- or band-pass frequency filtering cannot be performed, as there is no information beyond the current time, something that is usually required for such filtering. In this section I present a technique for monitoring and predicting the various tropical waves by a method of "real-time" filtering. It can be considered to be a form of one-sided filtering. For prediction of OLR anomalies, it demonstrates good skill for the MJO, and detectable (although possibly not very useful) skill for some of the other tropical waves. For the MJO, the technique compliments other methods of empirical prediction that have also been recently developed, in particular, those of Lo and Hendon (2000) and Waliser *et al.* (1999). Further, although the technique may not necessarily be better than what can be performed by subjective decisions of a human that is skilled at monitoring and predicting tropical intraseasonal variability, it is something that can easily be automated and used in hindcast experiments for examining the utility of such forecasts in a quantitative manner.

The method of the technique is to take the most recent year of OLR data at all longitudes, create anomalies with respect to the annual cycle (as calculated using the past 10 years), pad the end of the dataset with zeroes, and perform the wavenumber-frequency filtering with forward and inverse fast Fourier transforms (FFTs) independently at each latitude. No tapering is applied at the end of the dataset before the filtering, thus the filtered fields retain their amplitude up to the end-point. It is the part of the filtered fields that lead up to the end-point time that we call the real-time monitoring. The filtered fields that are returned from the FFT procedure for times beyond the end-point of the dataset (i.e., in the zero-padding) are used for the predictions. More details of the technique are provided in Wheeler and Weickmann (2001).
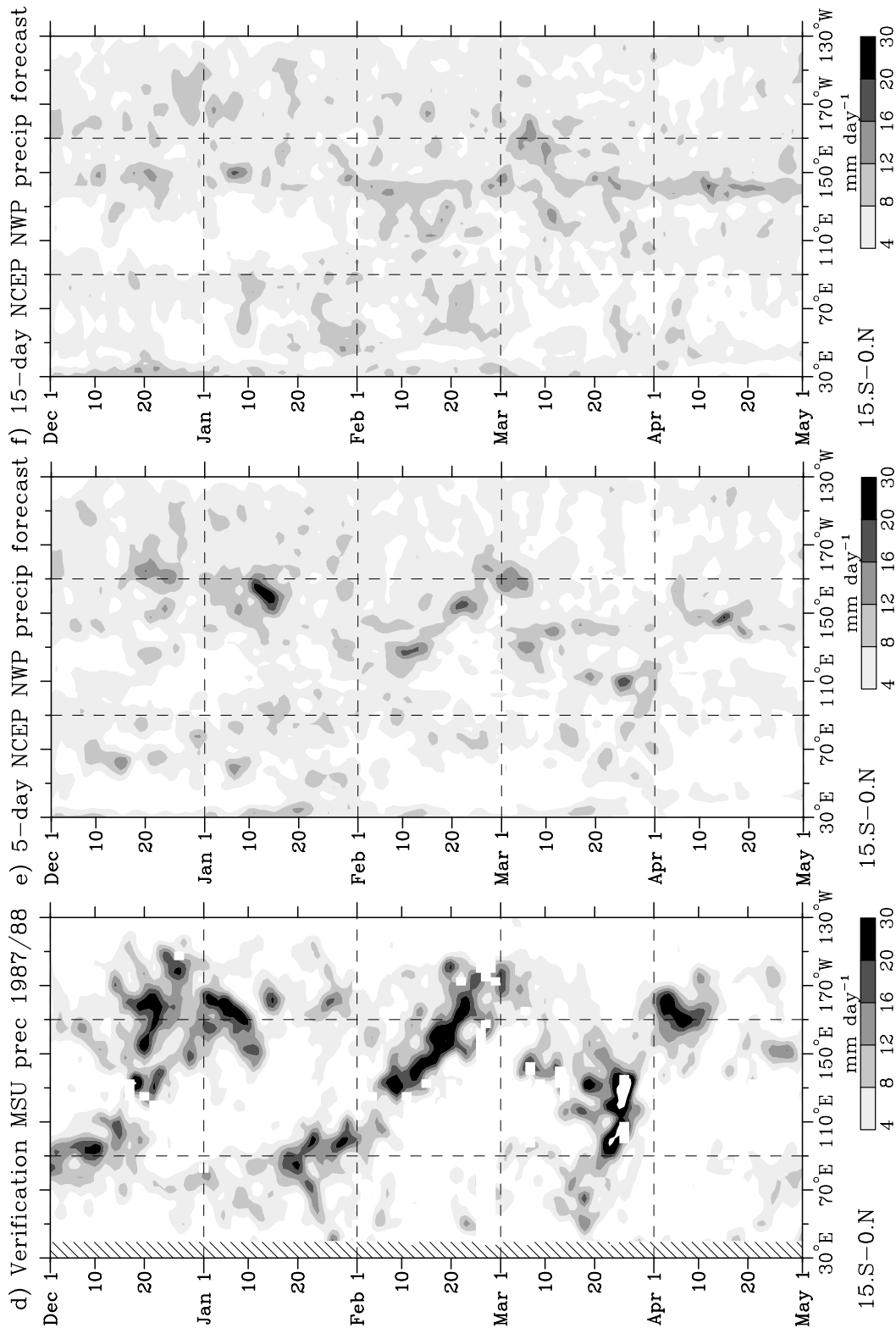
FIG. 21: (d) Time-longitude plot of (observed) MSU precipitation. Missing data is left blank and land areas hatched. A 1-2-1 filter has been applied in both space and time for smoothing purposes. (e) As in (d) except for 5-day forecasts of precipitation from the NCEP MRF model verifying on the days as labeled. (f) as in (e) except for the 15-day forecasts. (taken from Wheeler and Weickmann 2001).

Schematic of "real–time filtering" technique

OLR with seasonal cycle and trend removed at single location

"real–time filtering" forecast

OLR Anomalies

Longitude

Time

30 days

DAY 0

1 year of the most recent data

659 days of zero padding

Perform forward and inverse space–time FFTs on whole 1024 days and 145 longitudes to get thick line

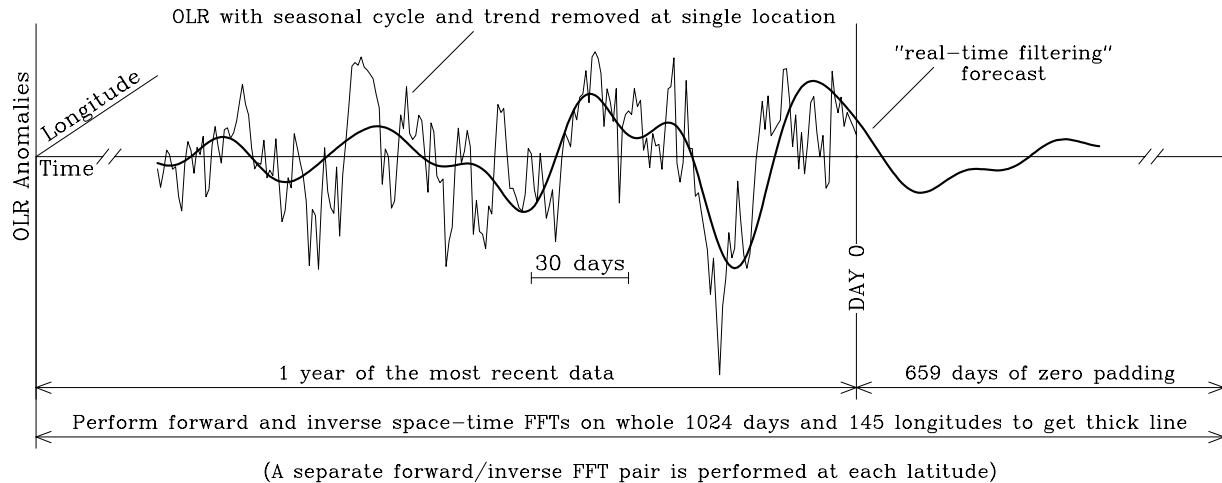(A separate forward/inverse FFT pair is performed at each latitude)

FIG. 22: Schematic of the procedure of real-time filtering for monitoring and prediction, as applied to a time series with an MJO-like signal. Note that in the actual procedure, two dimensions of information are used (taken from Wheeler and Weickmann 2001).

Fig. 22 presents a schematic of the procedure, as applied to the monitoring and prediction of a MJO-like signal. In this schematic, which shows the OLR data to be filtered at a single latitude/longitude location only, notice how the presence of a strong MJO-like signal near the end of the actual data continues as a signal in the filtered time series beyond the end-point of the dataset (i.e., into the zone that was padded with zeroes). Of course, this filtered signal is influenced by the presence or absence of a MJO-like signal at other longitudes as well. The end-point of the dataset is referred to as Day 0. In an operational setting, Day 0 would be the most recent 24-hour period in UTC time. The predicted OLR anomalies are with respect to the seasonal cycle and any variability acting on longer time scales. In this schematic, they can be seen to decay towards zero rather rapidly beyond day 0. Such decay is a general property of all such forecasts, something that a user must keep in mind. Further, although the schematic shows the forecast for a single mode of variability only, the real-time filtering procedure may efficiently produce a signal for each of the modes of variability labeled in Fig. 6.

An example of the technique applied to actual OLR data around the time of the onset of the Australian monsoon in late 1996 is provided in Fig. 23. The left-hand panel shows the total OLR field along with the diagnostically-filtered anomalies of the MJO and $n = 1$ ER waves. This filtering was performed using the entire dataset (i.e. up until 1999). The right-hand panel, on the other hand, shows the real-time filtering that was produced with the end-point of the dataset at the 5th of

December. In this presentation, the predictions are the filtered fields (i.e. the contours) that are presented for times beyond the 5th of December. Note that the contour interval used to plot the predicted anomalies has been halved relative to that used to plot the anomalies before Day 0, due to the known decaying property of the predictions by the technique.

Looking at the right panel, we see that the real-time filtering (as could have been produced on the 6th of December) is indicating that there is an enhanced phase of the MJO (solid contours) around 100°E, and it predicts that it should continue to propagate to the east. It also predicts an enhanced phase of the ER wave coming through at the same time. The technique also predicts that there should be suppressed convection associated with the MJO around 60°E from about the 10th to 20th of December. Now comparing this to what actually occurred (in the left panel), we see that in this case the real-time filtering performed quite well at providing a forecast of the future evolution of the OLR field for about 10 or more days ahead.

Showing the success of a single forecast, however, is not sufficient to verify a forecast technique. For this, many forecasts (or hindcasts) need to be made, and statistics need to be computed to indicate the true skill of the technique. Fig. 24 shows such a statistic for hindcasts of the MJO OLR that were computed for a 10-year period. The statistic shown is the anomaly correlation at each grid-point between the real-time filtered MJO OLR, and the diagnostically-filtered OLR (as calculated using the filtering without nearby end-points). The figure shows that during Southern summer the best fore-

a) Diagnostic filtering for Oct−Nov−Dec 1996

b) Real−time filtering for Dec 5th 1996
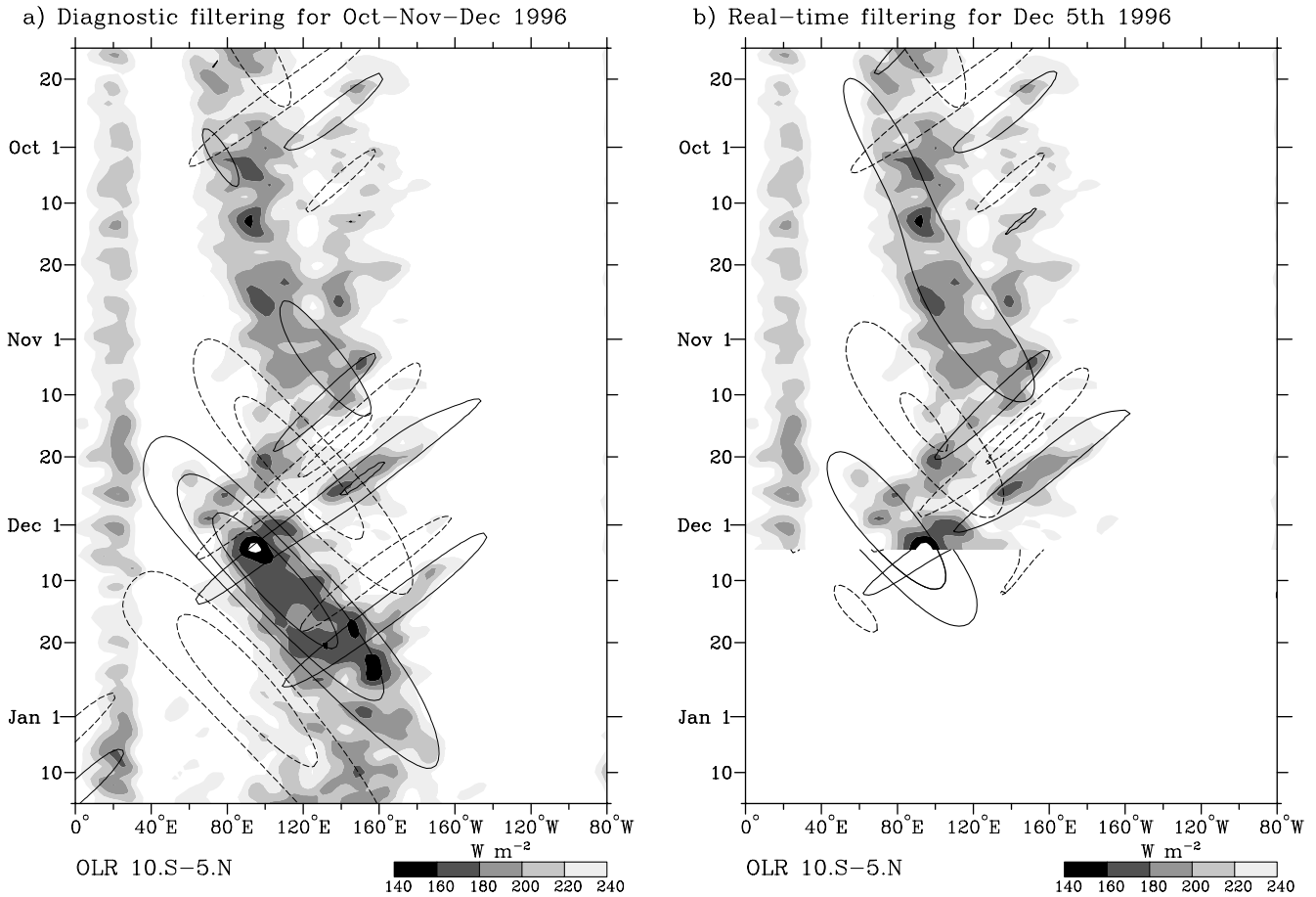
OLR 10.S−5.N

W m^{-2}

140 160 180 200 220 240

FIG. 23: (a) Time-longitude plot of the total OLR (with R21 spatial truncation, and a 1-2-1 filter applied in time) and filtered OLR anomalies averaged between 10°S and 5°N during late 1996 to early 1997. Shading is for the total OLR, and contours are for the diagnostically-filtered anomalies of the MJO and $n = 1$ equatorial Rossby (ER) wave. Solid contours represent negative OLR anomalies, while dashed contours are for positive anomalies, with the contour interval for both wave filtered bands being 10 W m^{-2}, and the zero contour omitted. (b) Same as (a), except that the filtering was performed with the last day of data being on December 5th, 1996. After December 5th, when the real-time filtered anomalies are continued into the future as a forecast, the contour interval is halved (taken from Wheeler and Weickmann 2001).

casts of the MJO are made in a region encompassing parts of northern Australia, Papua New Guinea, and across the southwest Pacific centred at a latitude of about 10°S. The correlations for the 15-day forecasts in these regions are greater than 0.6. For the opposite season, on the other hand, the best forecasts are made over the Indian ocean and northeastern Pacific. These correlations seem quite promising, although it must be remembered that they are only indicative of how much of the MJO portion of the variability that is being 'explained' by the predictions. When the correlations are computed against a field containing the total synoptic to intraseasonal variability of OLR, they are notably less, with peak values for a 15-day forecast around 0.3.

Finally, it is of note that the above statistics are cal-

culated during all years, and for the whole season. Yet it is known that the MJO, like other tropical waves, is not always occurring. Thus the statistics may be improved if calculated only for times when the MJO is determined to be relatively strong. It can be similarly shown that at times when one of the other tropical waves is particularly strong, empirical predictions of its phase by this real time filtering technique can also outperform a NWP prediction of precipitation.

8. Conclusion

A variety of well defined 'synoptic to intraseasonal' tropical waves exist in the tropical atmosphere. However, with the multitude of phenomena occurring at any
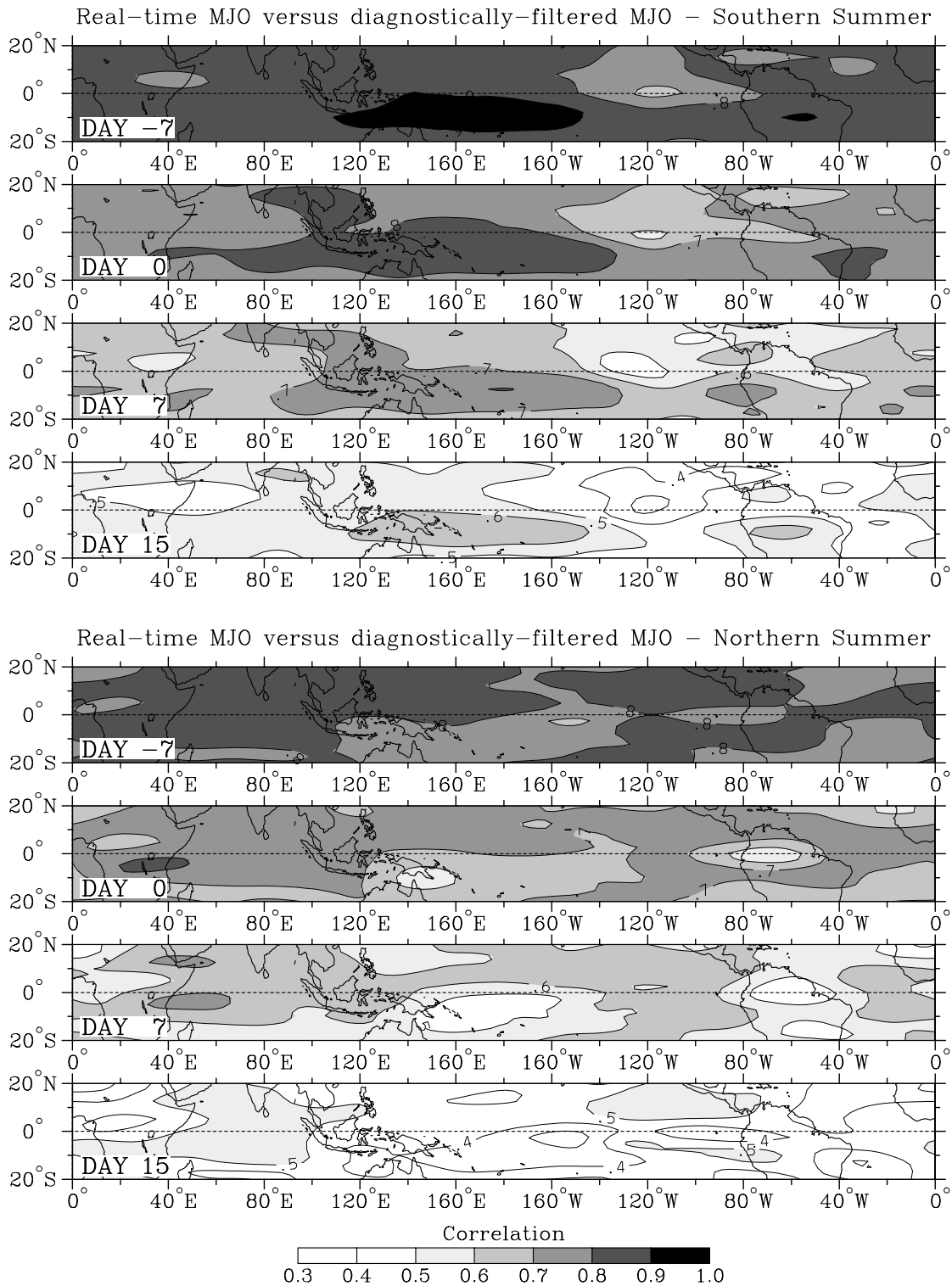
FIG. 24: Correlations of the MJO real-time filtered OLR with the validating diagnostically-filtered MJO OLR for southern summer (upper panels) and Northern summer (lower panels), for a number of lead times in days. Lead time is with respect to the end-point of the data input into the real-time filtering procedure as indicated in the lower left of each panel. All 10 years of the sample forecasts were used (taken from Wheeler and Weickmann 2001).

one time in the tropical atmosphere (e.g., numerous tropical waves, tropical cyclones, cold surges, monsoons, island convection etc.) it may be difficult to identify them in a standard synoptic analysis chart showing total fields only. Methods of real-time filtering may be

one way around this. For the MJO, real-time filtering of OLR has already been implemented in a semi-operational setting, and has shown some success for both monitoring and forecasting beyond the medium range (i.e. beyond several days). Until NWP mod-

els are able to better simulate the large-scale tropical waves, empirical methods such as the real-time filtering should be better placed for making such longer-range forecasts.

Acknowledgments

REFERENCES

Chang, C. P., 1970: Westward propagating cloud patterns in the tropical Pacific as seen from time composite satellite photographs. *J. Atmos. Sci.*, **27**, 133–138.

Gill, A. E., 1980: Some simple solutions for heat-induced tropical circulation. *Quart. J. Roy. Meteor. Soc.*, **106**, 447–462.

——, 1982: *Atmosphere-Ocean Dynamics*, Vol. 30, *International Geophysics Series*. Academic Press, 662 pp.

Holton, J. R., 1992: *An Introduction to Dynamic Meteorology*, 3rd ed., Vol. 48, *International Geophysics Series*. Academic Press, 511 pp.

Lo, F., and H. H. Hendon, 2000: Empirical extended-range prediction of the Madden-Julian oscillation. *Mon. Wea. Rev.*, **128**, 2528–2543.

Madden, R. A., and P. R. Julian, 1971: Detection of a 40-50 day oscillation in the zonal wind in the tropical Pacific. *J. Atmos. Sci.*, **28**, 702–708.

——, and ——, 1972: Description of global-scale circulation cells in the tropics with a 40–50 -day period. *J. Atmos. Sci.*, **29**, 1109–1123.

Matsuno, T., 1966: Quasi-geostrophic motions in the equatorial area. *J. Met. Soc. Japan*, **44**, 25–43.

Schemm, J. E., H. M. van den Dool, and S. Saha, 1996: A multi year DERF experiment at NCEP. *Preprints, 11th Conference on Numerical Weather Prediction*, Norfolk, VA. Amer. Meteor. Soc.. 47–49.

Sobel, A.H., and C.S. Bretherton, 1999: Development of synoptic-scale disturbances over the summertime tropical northwest pacific. *J. Atmos. Sci.*, **56**, 3106–3127.

——, and T. Horinouchi, 2000: On the dynamics of easterly waves, monsoon depressions, and tropical depression type disturbances. *J. Met. Soc. Japan*, **78**, 167–173.

Waliser, D. E., C. Jones, J.-K. E. Schemm, and N. E. Graham, 1999: A statistical extended-range tropical forecast model based on the slow evolution of the Madden-Julian oscillation. *J. Climate*, **12**, 1918–1939.

Weickmann, K. M., G. R. Lussky, and J. E. Kutzbach, 1985: Intraseasonal (30–60 day) fluctuations of outgoing longwave radiation and 250 mb streamfucntion during Northern winter. *Mon. Wea. Rev.*, **113**, 941–961.

Wheeler, M., and G. N. Kiladis, 1999: Convectively coupled equatorial waves: Analysis of clouds and temperature in the wavenumber-frequency domain. *J. Atmos. Sci.*, **56**, 374–399.

——, and K. M. Weickmann, 2001: Real-time monitoring and prediction of modes of coherent synoptic to intraseasonal tropical variability. *Mon. Wea. Rev.*, in press.

——, G. N. Kiladis, and P. J. Webster, 2000: Large-scale dynamical fields associated with convectively coupled equatorial waves. *J. Atmos. Sci.*, **57**, 613–640.